Journal of Molecular Liquids 346 (2022) 117856

Contents lists available at ScienceDirect

Journal of Molecular Liquids

journal homepage: www.elsevier.com/locate/molliq

Use of licorice plant extract for controlling corrosion of steel rebar in chloride-polluted concrete pore solution

R. Naderi [a,b,*], A. Bautista [b], F. Velasco [b,*], M. Soleimani [c], M. Pourfath [c]

[a] School of Metallurgy and Materials Engineering, College of Engineering, University of Tehran, P.O. Box 11155-4563, Tehran, Iran
[b] Department of Materials Science and Engineering, IAAB, Universidad Carlos III de Madrid, Avda. Universidad 30, 28911 Leganés, Madrid, Spain
[c] School of Electrical and Computer Engineering, College of Engineering, University of Tehran, Tehran, Iran

ARTICLE INFO

Article history:
Received 25 August 2021
Revised 8 October 2021
Accepted 14 October 2021
Available online 23 October 2021

Keywords:
Steel rebar
Licorice extract
Green corrosion inhibitor
Simulated concrete pore solution
Electrochemical assessment
Surface analysis

ABSTRACT

The possibility of using licorice extract as a green inhibitor for steel reinforcements in chloride-contaminated simulated concrete pore solution was explored in this study. Different licorice amounts were added to alkaline solutions and then 1% NaCl was also added. Electrochemical studies, up to 24 h, and surface analysis (X-ray photoelectron spectroscopy, Fourier transform infrared spectroscopy and scanning electron microscopy) were performed. Results demonstrated the inhibition effectiveness of the plant extract on steel rebar corrosion, regardless of the concentration, being detected an inhibition efficiency higher than 80 % with electrochemical techniques for 0.1% licorice extract, which showed the most effective performance. Surface analysis methods confirmed the presence of licorice on the surface, through the deposition of organic molecules present in the plant extract on the surface oxide/hydroxide. DFT calculations confirmed that compounds present in licorice can be chemically adsorbed on steel oxide surface.

1. Introduction

Corrosion of steel rebar in environments with chlorides is one of the main causes for failure of reinforced concrete structures [1]. The attack progresses through an autocatalytic mechanism and is quite aggressive [2], with the depth of the attack being determined by the microstructure [3]. The durability of reinforced concrete structures under this exposure conditions has tried to be extended by using galvanized reinforcements [4] or stainless steel reinforcements [5] in the most exposed areas of the structure, along with cathodic protection [6] and addition of corrosion inhibitors [7].

Although conventional synthetic inhibitors such as nitrites are capable of providing desirable corrosion control for reinforced concrete [7], their toxicity and carcinogenicity that cause temporary or permanent damage to the environment and to human health, have made it necessary to find green alternatives [8–11]. The most important ecofriendly candidates for replacing the toxic materials are the inhibiting species extracted from plant products [12–14]. These harmless natural products, which possess merits such as being readily available and biodegradable, are mainly composed of amino acids, tannins, terpenes, alkaloids, polyphenols and flavonoids. Significant amounts of N, O and/or S heteroatoms in these compounds create their potential to act as corrosion inhibitors [13,15,16]. Recently, relevant research has focused on inhibiting the corrosion of carbon steel rebar in chloride contaminated concrete using natural substances like extracted compounds from roots, seeds or leaves. Anitha et al. [17] introduced Rosa damascena leaf extract as a non-toxic anticorrosion material affecting rebar function in pore solution. These authors suggested the inhibitory action might result from deposition of a protective monolayer on the rebar surface hindering access of O_2 and chloride ions as depolarizing agents. Ginger extract was successfully employed by Liu et al. [18] to modify the corrosion resistance of reinforcements. As the inhibition mechanism, this mixed-type green inhibitor was reported to form an organic layer containing phenolic constituents on the bar surface, restraining anodic and cathodic zones. In another study, Zhang et al. [19] reported a corrosion inhibition efficiency up to 88.1 % for maize gluten meal. The anticorrosion behavior of this starch industry by-product was linked to adsorption on the rebar surface through amide groups. The corrosion inhibition effectiveness of turmeric extract on mild steel specimen in the simulated concrete pore solution, prepared in well water, was shown by Shanmugapriya et al. [20]. According to Left et al. [21], the *Chamaerops Humilis* L. leaves methanolic extract, by

* Corresponding authors at: Department of Materials Science and Engineering, IAAB, Universidad Carlos III de Madrid, Avda. Universidad 30, 28911 Leganés, Madrid, Spain.
E-mail addresses: rezanaderi@ut.ac.ir, rnaderi@ing.uc3m.es (R. Naderi), fvelasco@ing.uc3m.es (F. Velasco).

https://doi.org/10.1016/j.molliq.2021.117856
0167-7322/

enhancing the surface passive film, was able to provide an optimal inhibition efficiency of about 60% for steel reinforcement. Comparing the performance of the extract of Bambusa Arundinacea leaves to conventional amine and nitrite-based inhibitors in the concrete structure, Asipita et al. [22] indicated the superiority of the green inhibitor mainly due to pore plugging and hydrophobic properties. Extract of Olea europaea *L*., with a high content of inphenol and flavonoid, was shown to possess effective corrosion inhibitory properties for mild steel dipped into an alkaline solution simulating concrete when polluted with chlorides [23]. In order to combat chloride-induced reinforcement corrosion, Liu et al. [24] prepared a green inhibitor enriched with flavonoids and oligopeptides from waste *Platanus acerifolia* leaves. Their results revealed that the nitrogen-carbon layer formation is the main reason for the inhibitory action.

Licorice (*Glycyrrhiza glabra*) has been widely used in food and pharmaceutical industries. The extract of the sweet flavored yellow licorice root, which is considered a mixture with several bioactive constituents, has a variety of benefits [25–27]. It is well known that licorice extract is mainly composed of several triterpenes (e.g. glycyrrhizin and glycyrrhetic acid), flavonoids and various phenolic acids (e.g. liquiritigenin, licochalcone and glabridin) [28–31]. For instance, polyphenolic compounds such as tannins and flavonoids, which are found in abundance in licorice extract, are radical scavengers. In general, the naturally phytochemical substances with antioxidant/free radical scavenging characteristics based on their structure existing in plant extracts, are reported to have corrosion inhibitory ability [32]. Alibakhshi et al. utilized licorice extract as a highly efficient sustainable inhibitor to control corrosion of mild steel in neutral NaCl solution as well as 1 M HCl electrolyte [30,31]. The surface adsorption of organic molecules, present in the plant extract, was reported as the main reason the steel specimen corrosion was retarded in the acid solution. In the case of neutral electrolyte, protective layer formation at the interface of electrolyte/metallic plate was confirmed. In another research study, Deyab demonstrated the inhibition effectiveness of Egyptian licorice extract for copper in HCl [33]. The mixed-type inhibitory behavior was linked to the physical adsorption of some of the licorice extract's organic constituents. Despite investigations into the function of licorice extract in neutral and acidic media, no study in the literature on the applicability of this green inhibitor in the field of steel reinforcements was found. In order to clarify this issue, the influence of the licorice extract percentage on the steel rebar behavior exposed to chloride-polluted simulated concrete pore solution was monitored taking advantage of electrochemical methods. Insight into the performance of the green inhibiting species existing in the plant extract was provided by applying X-ray photoelectron spectroscopy (XPS) and scanning electron microscopy - energy dispersive X-ray spectroscopy (SEM-EDS) surface analysis as well as density-functional theory (DFT) quantum chemical calculations.

2. Materials and methods

2.1. Materials

The chemical composition of thermomechanically treated B400 corrugated steel bars of 8 mm diameter is presented in Table 1. The chemicals (including NaOH, $Ca(OH)_2$, KOH and NaCl) were all supplied by Panreac Co. and used with no further purification.

For aqueous extraction of the licorice root, collected from the northeast of Iran, 30 g of the small parts of the ambient temperature-dried plants was magnetically stirred for 3 h at 70 °C. After filtration, the clear yellow solution was put in an oven at 60 °C to be dried for 24 h. Different concentrations of the extract (0.025, 0.05, 0.075 and 0.1 wt%) were introduced to the simulated concrete pore solution including KOH, NaOH and $Ca(OH)_2$. In detail, the blank alkaline electrolyte was prepared with the addition of 0.3 M KOH and 0.1 M NaOH to deionized water. The solution was then saturated with $Ca(OH)_2$ and filtered.

2.2. Methods

2.2.1. Electrochemical examination

The licorice extract inhibitory function was assessed through electrochemical impedance spectroscopy (EIS) and polarization techniques employing a Gamry Reference 600 potentiostat/galvanostat. The three electrodes, implemented in the electrochemical test setup, were spiral stainless steel wire, saturated calomel electrode (SCE) and acetone degreased bar as counter electrode (CE), reference electrode (RE) and working electrode (WE), respectively. In order to prevent formation of differential aeration cells in the measurement, the bottom and the surface of the corrugated bars close to the solution level were sealed with epoxy paint, leaving an area of 3 cm in length for vertical exposure to the chloride contaminated alkaline electrolyte. Furthermore, it is important to note that the core had a different microstructure compared to the outer martensitic layer of the bars, causing different corrosion behaviors. To record AC impedance spectra as Nyquist and Bode plots at open circuit potential (OCP) in the frequency range of 10000–0.01 Hz, a perturbation of 10 mV of amplitude was used. The WE preparation procedure for the EIS test was to immerse the bars in the simulated concrete pore solutions with different licorice extract contents for 1 h. Then, 1 wt% NaCl was added to the electrolyte. The AC impedance spectra were acquired after 1, 4 and 23 h exposure to the chloride contaminated electrolyte. Taking into account 1-h pre-dipping into the inhibited electrolyte with no chloride, the total immersion periods were actually 2, 5 and 24 h. Moreover, bars were tested in chloride solution without licorice. The reference bars (blank specimens) for electrochemical measurements were prepared through 1-h pre-immersion into the alkaline electrolyte with no additive (inhibitor and chloride), and then 23 h dipping into the simulated concrete pore solutions with NaCl. In all cases, stagnant solutions were used, as typically done when testing under simulated concrete pore solutions, to avoid changes in corrosion mechanisms due to changes in the amount of dissolved gases (increasing the dissolved O_2 that reaches the rebar surface can alter meaningfully the conditions where the degradation of the rebars embedded occurs). At least three samples were evaluated in each solution. To fit the spectra and extract the parameters, ZSimpWin software was used in this work. The polarization curves, in the potential range of ± 300 mV vs. OCP, were acquired at the scan rate of 1 mV/s. All the electrochemical measurements were made at room temperature (20–25 °C) and repeated three times to ensure repeatability.

2.2.2. Surface characterization

The SEM-EDS (Teneo-LoVac equipment, Thermo Fisher Scientific Inc.) and XPS (Specs EA 10 Plus device) techniques were employed to analyze the specimen surface morphology, composi-

Table 1
Chemical composition (wt. %) of the carbon steel reinforcements studied in this work.

C	S	P	Si	Mn	Cr	Cu	Mo	Ni	Fe
0.13	0.022	0.006	0.23	0.54	0.15	0.44	0.02	0.12	Bal.

tion and chemical bonds after 24 h exposure at room temperature (20–25 °C). XPS analyses were carried out in VG Scientific Microtech Multilab equipment, at a residual pressure below $5{\cdot}10^{-8}$ Torr. A survey scan encompassing the 0–1200 eV region was obtained for each sample, and high-resolution spectra were obtained for C, O and Fe peaks. All binding energies were referred to the C (1 s) core level spectrum position at 285 eV. The attenuated total reflection-Fourier transform infrared (ATR-FTIR) analysis of the licorice extract powder was conducted between 400 cm^{-1} and 4000 cm^{-1}. Moreover, the ATR-FTIR spectrum of the sample surface after 24 h of exposure to the electrolyte containing 0.1 % of the plant extract was also gathered to assess the surface deposition of inhibiting species.

2.2.3. DFT computational details

The electronic properties for inhibitor components under vacuum conditions were calculated based on DFT calculations, by using the Gaussian code [34] with B3LYP/6–31++G**-D2 exchange correlation (XC) functional. The electronic properties are described by the energy levels of the highest occupied molecular orbital (E_{HOMO}), the lowest unoccupied molecular orbital energy (E_{LUMO}), energy bandgap ($\Delta E = E_{LUMO} - E_{HOMO}$), dipole moment ($\mu$), electronegativity ($\chi = -0.5(E_{HOMO} + E_{LUMO})$), global hardness ($\eta = -0.5(E_{HOMO} - E_{LUMO})$) and the maximum number of transferred electrons $\Delta N_{max} = \chi/2\eta$. The electronic structure calculations of Fe_2O_3(0001) unit cell were carried out with the frozen-core projector augmented wave (PAW) [35], the generalized gradient approximation (GGA) and Perdew, Burke, Ernzerhof (PBE) XC [36] as implemented in the Vienna *ab initio* simulation package (VASP) code [37,38]. The solvent effect was considered by using the implicit water solvent model implemented in VASPsol [39]. The long-range van der Waals (vdW) interaction is described by the DFT-D3 approach [40,41]. The DFT calculations were corrected for the on-site Coulomb interaction (Hubbard U) for the d electrons within the DFT + U [42–44]. By using a U-J value of 4.3 eV [45], the excess electrons were correctly localized at Fe sites instead of being delocalized at many Fe atoms. The cutoff energy is 550 eV. For the 2D Brillouin zone sampling, a (8 × 8 × 1) Monkhorst − Pack k point was chosen. The structure optimizations were performed until the residual force and energy difference become smaller than 0.01 eV $Å^{-1}$ and 10^{-5} eV, respectively. For M (H_2O, OH and Cl) adsorbate, the adsorption free energies are given by:

$$\Delta G_{ads} = G_{Substrate-M} - (G_{Substrate-M})_{away} \quad (1)$$

The free energy is defined as:

$$G = E + ZPE - TS \quad (2)$$

where E is the total energy of species, S is the entropy and ZPE is the zero-point energy at room temperature.

The metal facet structure of Fe_2O_3 (4 × 3 × 1) super cell with fixed layers was considered for the adsorption of inhibitor components. In order to avoid interactions between layers, the vacuum was set to 20 Å. As the model for water content in neutral conditions, the interface was made with 24 water molecules in three layers that can freely move during simulation [46,47]. The 5 hydroxyls were substituted by the same number of water molecules in the case of the alkaline solution. An additional immobile buckled hexagonal water layer was placed at the top of the mobile water molecules to fix the density of water at the interface. *Ab initio* molecular dynamic (AIMD) simulations were performed at a constant temperature of 300 K under the NVT ensemble. The temperature was controlled by the weak coupling of Nose-Hoover thermostat [48]. The simulation time for each unit cell was 0.5 ps with a time step of 1 fs.

3. Results and discussion

3.1. Electrochemical assessment

Fig. 1 presents the output of EIS assessment as Nyquist and Bode curves of the corrugated bars exposed to simulated concrete pore solutions with different percentages of the licorice root extract. One of the most important features revealed in the curves is the significant impact of the green inhibiting species dosage on the specimen behavior, meaning that the increase in the licorice extract content caused an extension in the Nyquist loop radii and a shift of the low frequency impedances in the Bode diagrams to higher values. In other words, since the loop diameter indicates the polarization resistance, the superiority of licorice 0.1 % (the highest percentage) and the inferiority of licorice 0.025% (the lowest percentage) was obvious from the Nyquist curves. The order of corrosion inhibition, Licorice 0.1% > Licorice 0.075% > Licorice 0.05% > Licorice 0.025% > Blank, can be drawn from the low frequency impedance values in the Bode diagram as well. The order was more obvious after 24 h dipping, probably due to gradual adsorption of the organic molecules existing in the extract on the bare specimen surface. A similar appearance of the spectra may reflect no significant difference in the corrosion behavior of various specimens under study [19]. To top it off, regardless of the percentage, the corrosion of bars exposed to the alkaline solutions containing licorice extract was more or less controlled, indicating this green additive's effectiveness. When the dipping time increased, the capacitive arc radii decreased, indicating an increase in the corrosion current density. Despite the drop in the chloride-induced corrosion resistance within immersion time for all the samples, the alkaline solution with 0.1% licorice extract was able to retain its superiority, which suggests the significant impact of this green inhibitor dosage on the surface oxide film reinforcement.

To analyze the bars' AC impedance spectra in the blank electrolyte as well as in inhibiting alkaline solutions, the ZSimpWin software with a simple R(RQ) equivalent circuit was employed. The equivalent circuit including solution resistance (R_s), charge transfer resistance (R_{ct}) and double layer constant phase element (CPE_{dl}) was selected on the basis of detecting only one time constant in the Bode diagrams as well as a single capacitive semicircle in the Nyquist plots during the whole dipping period. All plots revealed frequency depression or deviation from ideal semicircle performance probably because of the heterogeneity and roughness of the specimen surface within corrosion reactions [49,50]. Accordingly, constant phase element introducing characteristic parameters of admittance (Y_0) and frequency exponent (n) was used as a component of the equivalent circuit instead of ideal capacitance. Table 2 summarizes some data drawn from the spectra of various samples under study after fitting them with a one-time constant equivalent circuit. In this table, **Eq. 1** was used to calculate the parameter C_{dl} [51]. The time and extract concentration dependency of inhibition efficiency (IE), which was calculated using **Eq. 2** [52], is illustrated in Fig. 2. The parameters $R_{t,inh}$ and $R_{t,b}$ in the equation represent the total resistances of the inhibited specimen and the blank one, respectively.

$$C_{dl} = {Y_0}^{1/n}\left(\frac{1}{R_s} + \frac{1}{R_{ct}}\right)^{\frac{n-1}{n}} \quad (1)$$

$$IE(\%) = \left(\frac{R_{t,inh} - R_{t,b}}{R_{t,inh}}\right) \times 100 \quad (2)$$

The R_{ct} trend and magnitude reflected the inhibition effectiveness of the licorice extract, particularly the dosage of 0.1%. This suggested that the organic moieties in the plant extract are able to strengthen the electrolyte/steel bar interface through absorbing

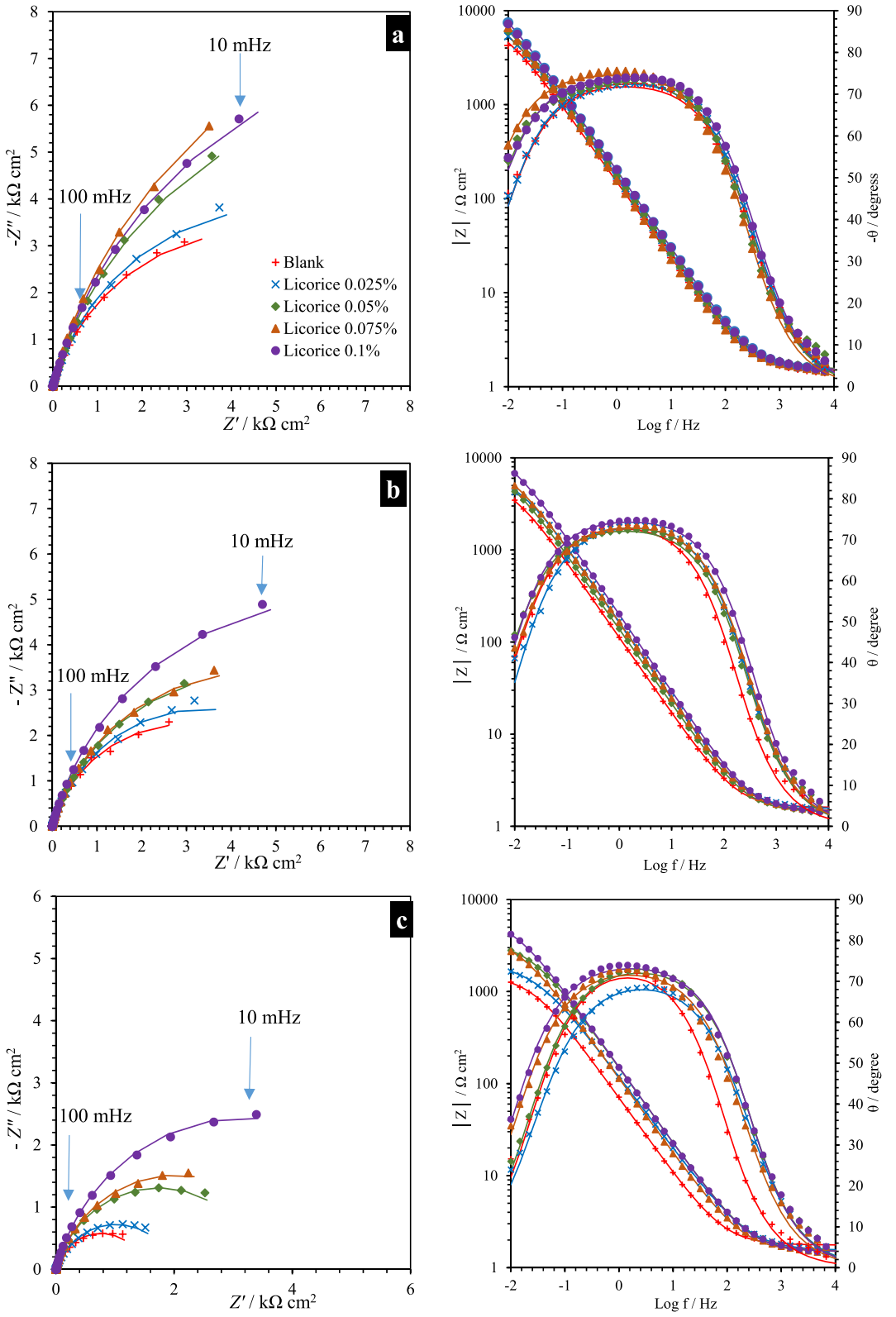

Fig. 1. The effect of the concentration of licorice extract on the EIS assessment output for the bars exposed to simulated concrete pore solution for (a) 2, (b) 5 and (c) 24 h; the solid lines correspond to the fitted data.

on the surface. Moreover, the values of R_{ct} during the dipping period indicated that an increase in the extract content resulting in an increase in the amount of organic inhibiting species in the alkaline electrolyte can intensify the interface reinforcement as the highest inhibition efficiency (81 %) was achieved for the sample with the greatest concentration of extract. Although the charge transfer resistance revealed a descending trend as time elapsed, the corrosion inhibition order remained unchanged until 24 h. The influence of the extract on the interface can be also deduced from the C_{dl} whose values for the electrolyte with no additive were higher than

Table 2
The data resulting from fitting of the impedance spectra of samples containing different concentrations of licorice extract with a one-time constant equivalent circuit.

Sample	Immersion time (h)	R_s (Ω cm^2)	R_{ct} (kΩ cm^2)	CPE		C_{dl} (μF cm^{-2})	Chi square	E vs. SCE (mV)
				n	Y_0 (mΩ^{-1} cm^2 s^n)			
Blank	2	1.41	8.9 ± 0.8	0.82 ± 0.01	2.3 ± 0.1	689 ± 149	8.6E-4	−301 ± 8
	5	1.60	5.2 ± 0.7	0.81 ± 0.01	2.5 ± 0.3	683 ± 115	1.2E-3	−405 ± 15
	24	1.76	1.3 ± 0.2	0.82 ± 0.01	2.8 ± 0.2	932 ± 131	8.1E-4	−496 ± 11
Licorice 0.025%	2	1.48	1.2 ± 0.2	0.82 ± 0.01	1.8 ± 0.2	528 ± 98	2.5E-3	−293 ± 5
	5	1.55	6.5 ± 0.4	0.82 ± 0.02	1.7 ± 0.2	491 ± 43	1.2E-3	−346 ± 5
	24	1.54	2.4 ± 0.3	0.79 ± 0.01	2.6 ± 0.2	648 ± 118	7.6E-4	−463 ± 13
Licorice 0.05%	2	1.54	17.3 ± 0.8	0.81 ± 0.01	1.9 ± 0.1	498 ± 27	8.6E-4	−272 ± 3
	5	1.42	9.3 ± 0.6	0.82 ± 0.01	1.5 ± 0.2	368 ± 46	7.8E-4	−331 ± 9
	24	1.50	3.2 ± 0.3	0.82 ± 0.01	1.5 ± 0.1	446 ± 20	1.1E-3	−448 ± 5
Licorice 0.075%	2	1.52	22.3 ± 1.3	0.82 ± 0.01	1.3 ± 0.1	356 ± 58	8.3E-4	−259 ± 10
	5	1.47	9.0 ± 0.3	0.83 ± 0.01	1.4 ± 0.1	424 ± 62	1.8E-3	−299 ± 11
	24	1.50	4.6 ± 0.6	0.81 ± 0.01	2.1 ± 0.3	544 ± 16	1.6E-3	−421 ± 4
Licorice 0.1%	2	1.51	19.7 ± 1.3	0.82 ± 0.01	1.2 ± 0.2	331 ± 41	7.2E-4	−254 ± 6
	5	1.45	11.7 ± 1.6	0.83 ± 0.01	1.2 ± 0.1	333 ± 27	6.8E-4	−308 ± 8
	24	1.50	6.8 ± 0.7	0.81 ± 0.01	1.4 ± 0.1	376 ± 25	9.6E-4	−410 ± 8

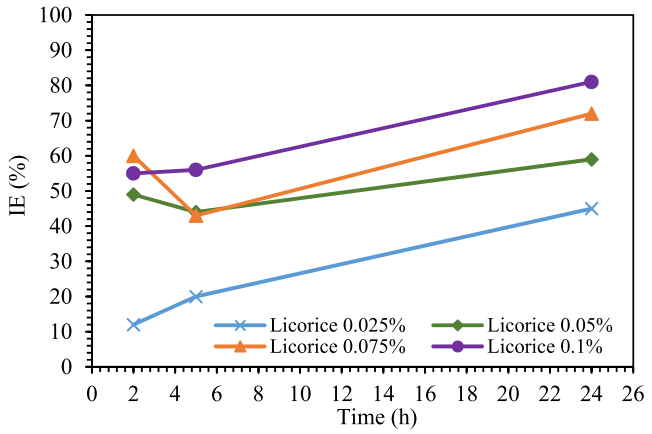

Fig. 2. Time variation of inhibition efficiency of different concentrations of licorice extract.

those for the inhibited solutions within the whole dipping time, probably due to adsorption of the inhibiting species restricting the water molecules diffusion into the surface film [53,54]. For instance, the C_{dl} value of the blank specimen at the end of dipping time was about 2.5 times higher than that of the bar exposed to the alkaline solution contaminated with 0.1% licorice root extract. The last column of Table 2, presenting the OCP variation during the test period, can reflect the role of licorice extract as corrosion inhibitor. In other words, the potential values were less negative in the presence of the plant extract compared to the blank solution. Moreover, among the inhibited solutions those contaminated with lower dosages of licorice extract possessed more negative OCPs. From Fig. 2, the trend of IE for different dosages of the plant extract revealed that the organic inhibiting species adsorption on the bar sample surface is time consuming [55]. Comparing the IE values after 2 and 24 h in all cases, one can observe the gradual surface adsorption of organic molecules existing in the licorice extract.

Although it is difficult to stablish a comparison, the IE values (Fig. 2) are in accordance to those obtained in chloride simulating-concrete solutions (above 80%), using other inhibitors based on plant extract. The use of Rosa damascena leaf extract [17] in 0.5 M NaCl is able to provide 81.6% efficiency, while 2 g/L maize gluten meal [19] in 3% NaCl solution offers 88.1% efficiency,

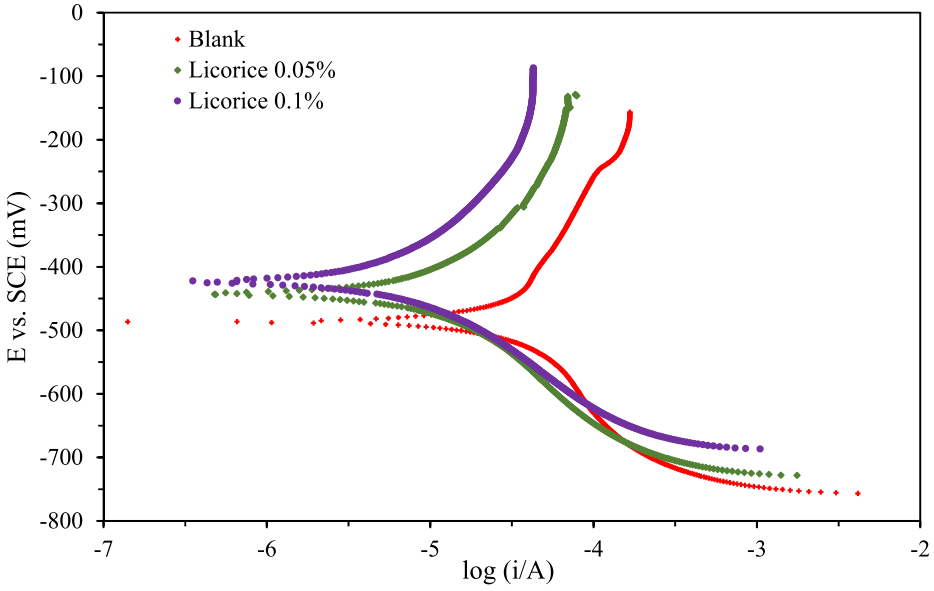

Fig. 3. Polarization curves of the bars after 1 h exposure to simulated concrete pore solutions containing 0, 0.05 and 0.1 wt% licorice extract and then 23 h immersion in the chloride contaminated electrolytes.

always using R_{ct} as parameter to measure the efficiency (as in this work). However, it is important to point out that those studies do not consider the real surface of the reinforcements, but sand-finished steel samples. The use of corrugated bars, as it is done in the present study, is advisable, as the surface of the carbon steel reinforcements has a specific microstructure that determines their corrosion performance [3,56].

Fig. 3 illustrates the polarization curves of the specimens after 1 h dipping in the simulated concrete pore solutions with 0, 0.05 wt% (middle concentration) and 0.1 wt% (highest concentration) licorice extract and then 23 h immersion in the chloride contaminated solutions. This indicates the consistency of the order of inhibitory abilities (the higher the licorice percentage, the more effective the inhibition) with those detected from the EIS data. Analysis of the curves via Tafel extrapolation resulted in obtaining some parameters including i_{corr} (corrosion current density), b_c (cathodic Tafel slope), b_a (anodic Tafel slope) and E_{corr} (corrosion potential) which are listed in Table 3. The IE (inhibition efficiency) values of 57% and 74% respectively for the samples Licorice0.05% and Licorice0.1% were obtained based on the ratio of the difference between the i_{corr} values of uninhibited solution and each electrolyte with extract to the i_{corr} value of the electrolyte without extract, multiplied by 100 [57]. It is clear that both IE values (from EIS, Fig. 2, and polarization) were coherent. A mixed-type inhibitor was deduced from the polarization data because of the drop in the corrosion current density shift as well as the change in b_c and b_a as the licorice extract was introduced. Both anodic and cathodic branches were affected with the addition of licorice. Moreover, since the E_{corr} difference between blank and inhibited electrolytes was lower than 85 mV, we are not able to classify the inhibitor as a solely cathodic or anodic type [58]. Other plant extracts behave in the same manner (as mixed-type corrosion inhibitors) [17–19] in chloride simulated concrete solutions. This behavior was suggested to have arisen from precipitation of the organic moieties existing in the extract on the bar surface, strengthening the oxide film. The corrosion current density and inhibition efficiency values

Table 3
The data resulting from analysis of the polarization plots of the bars after 1 h exposure to simulated concrete pore solutions containing 0, 0.05 and 0.1 wt% licorice extract and then 23 h immersion in the chloride contaminated electrolytes.

Sample	i_{corr} (μA cm^{-2})	E_{corr} (mV vs SCE)	b_a (mV)	b_c (mV)
Blank	32	−489	447	261
Licorice 0.05%	13.5	−444	334	244
Licorice 0.1%	8.3	−422	333	185

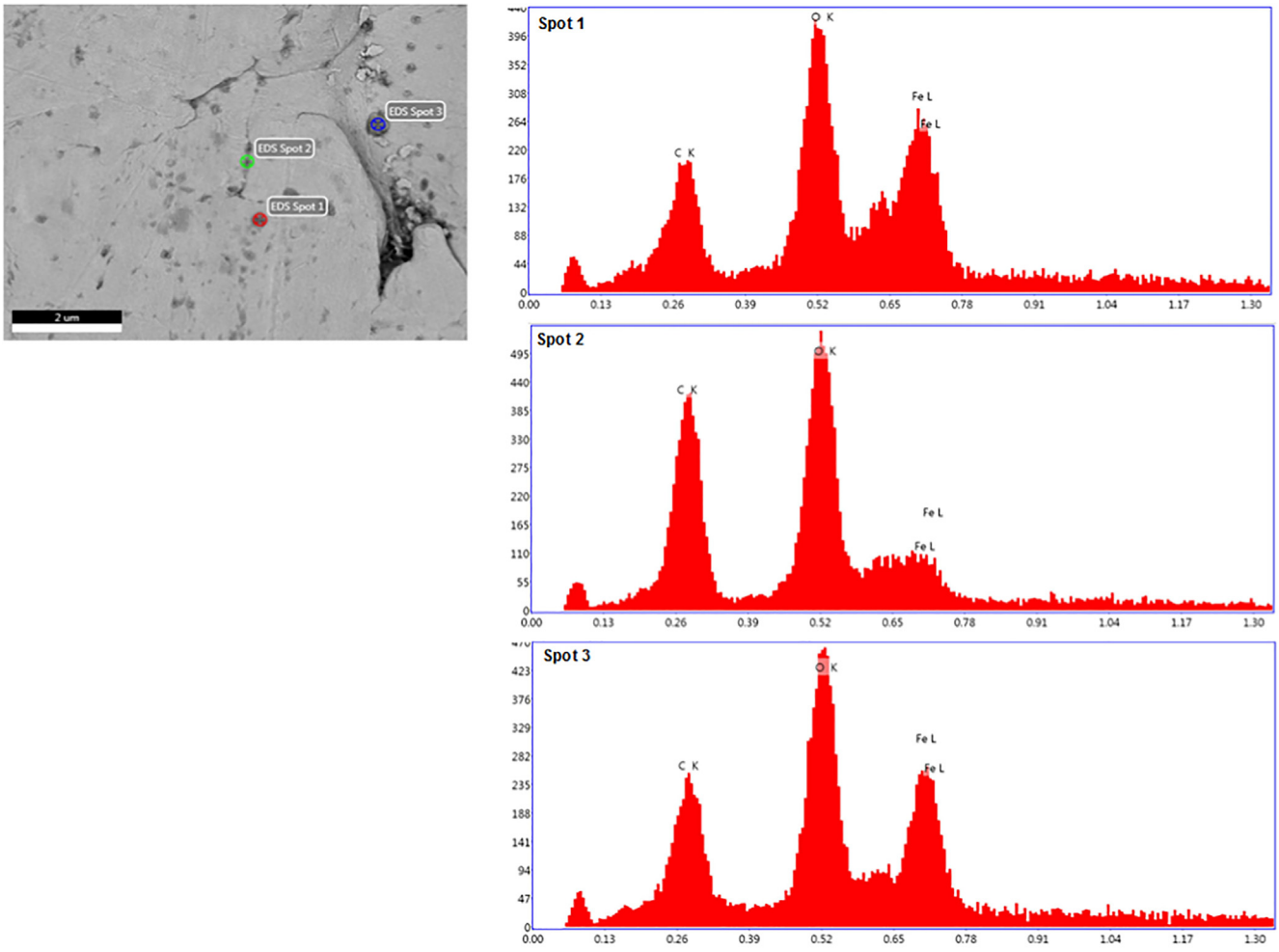

Fig. 4. The SEM-EDS assessment output of the specimen surface exposed to the alkaline electrolyte containing licorice extract for 24 h.

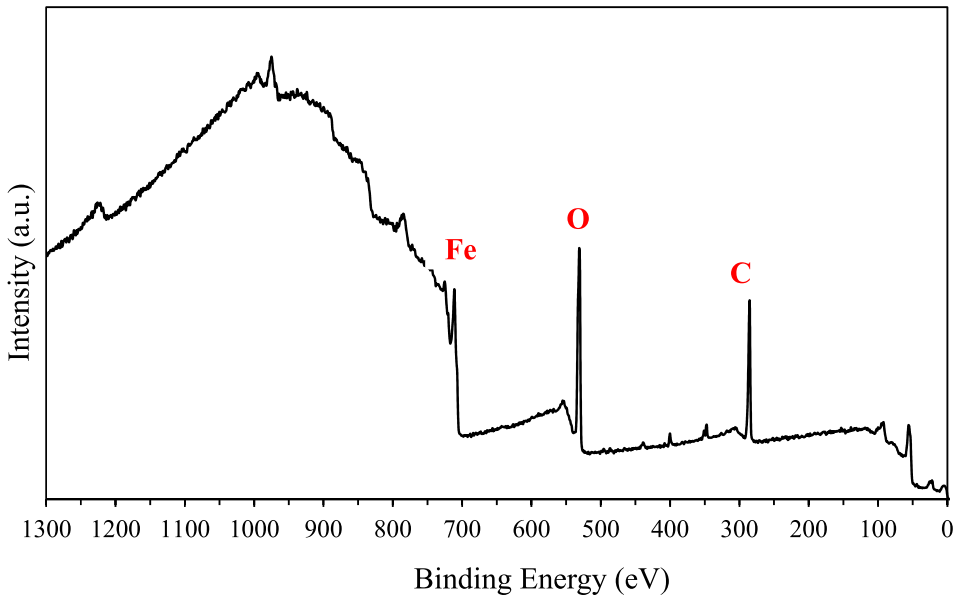

Fig. 5. XPS survey spectrum taken from the steel rebar surface exposed to the alkaline electrolyte containing licorice extract for 24 h.

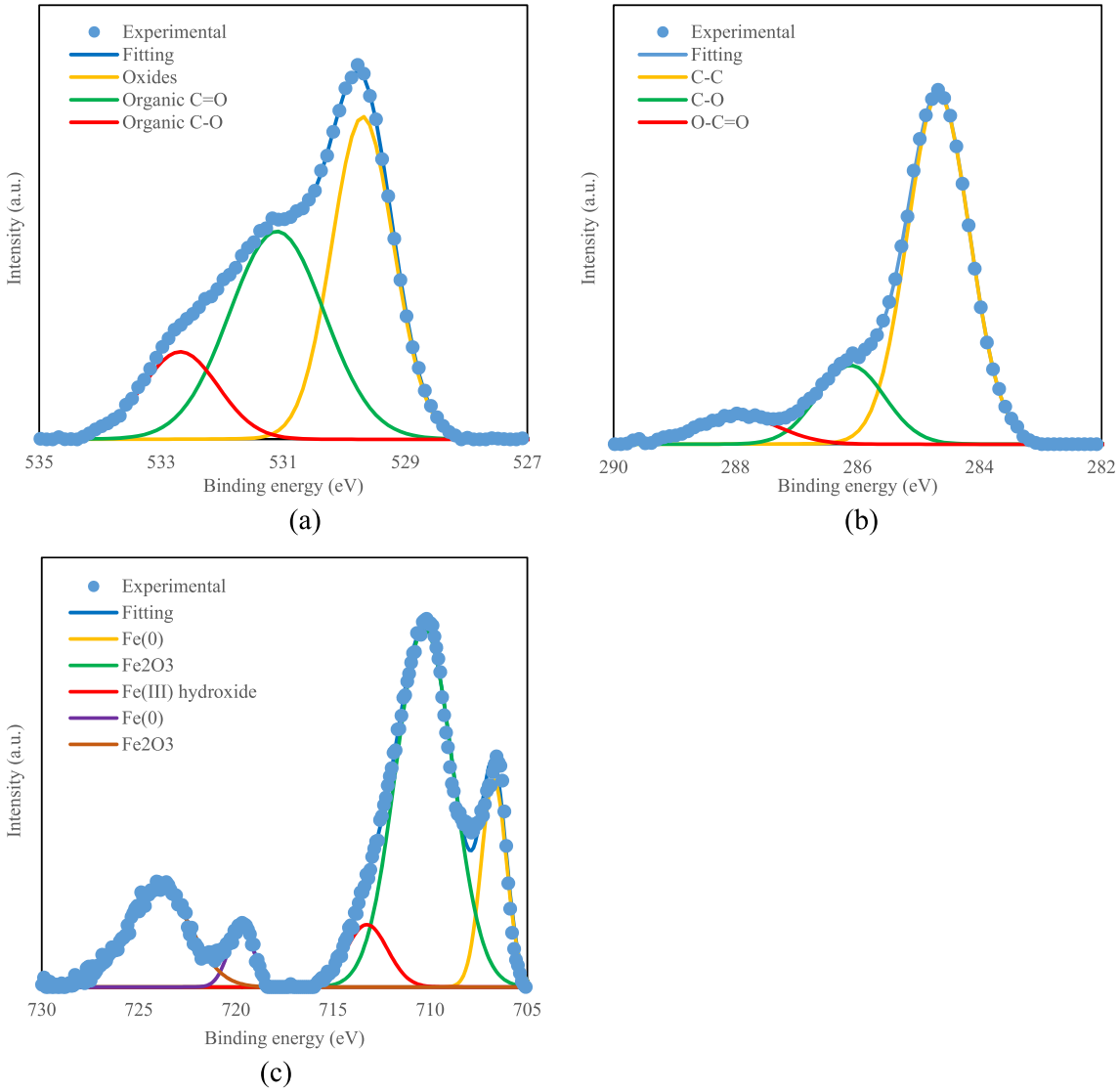

Fig. 6. XPS deconvolutions for the O 1 s (a), C 1 s (b) and Fe 2p (c) peaks of a carbon steel immersed for 24 h in the alkaline electrolyte containing licorice extract.

decreased and increased respectively in the case of the sample licorice 0.1% compared to the sample licorice 0.05%, probably in response to an enhancement in the chance of film formation on active zones as liberated organic molecules increased.

3.2. Surface characterization

The output of SEM-EDS analysis on the specimen surface after 24 h dipping in the alkaline solution containing chloride ions and licorice extract is presented in Fig. 4. Some important features can be inferred from this surface analysis. At first glance, the surface was found to be covered by a compact film. Considering detection of Fe and a significant amount of oxygen in the EDS assessment, one can deduce that the specimen surface is oxidized and covered by an oxide/hydroxide layer. Additionally, the presence of carbon and oxygen in different spots of the surface can confirm the speculation made in evaluating of the electrochemical behavior of specimens exposed to the inhibited alkaline solution on the contribution of organic molecules in the licorice extract to reinforcement of the surface oxide film.

An XPS study was performed to analyze the outer layer of the steel after 24 h immersion in the licorice containing solution. Consistent with the EDS surface analysis result, the XPS measurement, whose survey spectrum is depicted in Fig. 5, indicated the presence of three main peaks of Fe, O and C on the steel rebar surface exposed to the alkaline electrolyte containing licorice extract.

Fig. 6 shows the spectra of C 1 s, O 1 s and Fe 2p of carbon steel surface, with the peak deconvolution results. Both the C and O peaks were deconvoluted into 3 components, as shown in Table 4. The C component at 284.7 eV could be related to adventitious carbon, although its aliphatic character may also be related to species coming from licorice extract in the solution [59]. The other two C contributions represented 26% of the peak area, and were clearly present in the structure of different components of licorice. The assignment of these C components to licorice extract can also be understood if the C 1 s spectrum of the same steel after immersion in the same solution without licorice is taken into account (Fig. 7). Although again three C components can be found, the one related to O-C = O did not appear, and a strong signal of carbonates (positioned at 289.2 eV [60]) was found. Moreover, the area of the C 1 s peak of steel in licorice solution was almost double (1.85 times) that of the steel in the blank solution. The assigned bonds in C 1 s spectrum were also found in O 1 s peak (Fig. 6). Together with the typical organic bonds, C-O and C = O, oxides were also present. The presence of those organics can match the previously mentioned speculations about deposition of organic molecules present in licorice extract on the surface oxide playing an important role in strengthening the film. The Fe 2p spectrum fitting (Fig. 6**c**) resulted in five subpeaks, listed in Table 4. The appearance of the metallic iron signal (706.7 and 719.4 eV for Fe $2p_{3/2}$ and $Fe2p_{1/2}$ respectively) might be an indication of passive film with a thickness < 10 nm, due to the XPS maximum depth detection

Table 4
Position of all components detected in the XPS fitting of C 1 s, O 1 s and Fe 2p signals.

Peak		Position (eV)	Assignment	Reference
C 1 s		284.7	C-C	[59]
		286.1	C-O	[63]
		288.0	O-C = O	[59,64]
O 1 s		529.7	Oxides	[18]
		531.1	Organic C = O	[65,66]
		532.7	Organic C-O	[65]
Fe 2p	$Fe2p_{3/2}$	706.7	Fe(0)	[61]
		710.3	Fe_2O_3	[62,67]
		713.3	Fe(III) hydroxide	[68]
	$Fe2p_{1/2}$	719.4	Fe(0)	[69]
		723.7	Fe_2O_3	[67]

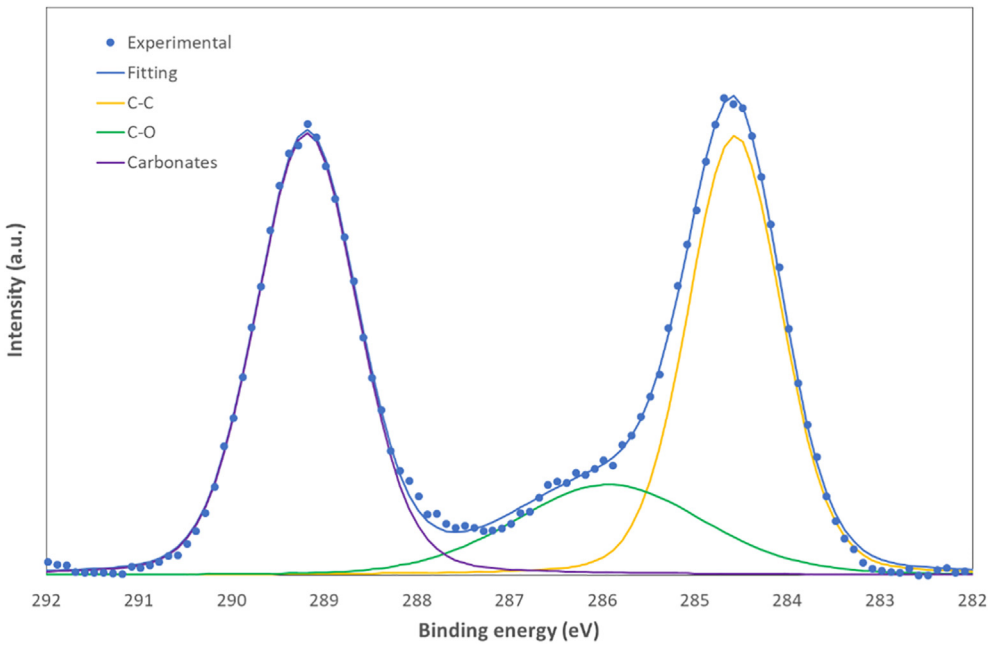

Fig. 7. XPS deconvolution for the C 1 s peaks of a carbon steel immersed for 24 h in the alkaline electrolyte with no licorice extract.

[61]. Appearance of two signals at about 710.3 and 723.7 eV might be related to the Fe (III) oxide phase formation [62]. The presence of $Fe(OH)_3$ can be detected from the signal at 713.3 eV. As a consequence, assessment of the Fe 2p XPS spectra showed that a composite of iron oxides and hydroxides was formed on the surface.

Moreover, the FTIR assessment data of licorice extract powder (Fig. 8) as well as the FTIR-ATR spectrum of carbon steel surface after immersion in the licorice containing solution (Fig. 9) could support other characterization results. At first glance, the licorice extract appeared to contain a variety of functional groups (e.g. carboxyl, hydroxyl and carbonyl), increasing the chance to play a role as a corrosion inhibitor. Comparing the two spectra in Figs. 8 and 9, one can observe the signal of licorice on the steel surface. The assignments of bands (Table 5, [70,71]) showed the presence of bonds that can be easily correlated to the organics found in the components of licorice, which have been adsorbed on the surface. However, it must be pointed out that data at energies below 900 cm^{-1} can also be related to different substitutions in the aromatic groups, in accordance with the complexity of licorice molecules/components, instead of the rocking of $–CH_2–$ as stated in Table 5. Other small signals in the range 1450–1050 cm^{-1}, not included in Table 5, can be identified with other bonds (such as–C = O), also present in licorice components.

3.3. DFT calculations

Since inhibitor microscopic properties are important for inhibition response in corrosion , [72–76] the quantum chemical parameters of licorice compounds were assessed and are presented in Table 6. Higher values of E_{HOMO} and lower values of E_{LUMO} that lead to strong electron donation and acceptance of inhibitor, respectively, are suitable indicators of potential inhibition efficiency. In addition, a smaller energy bandgap and a larger dipole moment in inhibitor components result in a higher chemical reactivity and lower kinetic stability of inhibitors on the substrate [75,76]. A larger difference in the electronegativity is a driving force for electron transfer, whereas a larger sum of hardness parameters acts in the opposite way. Overall, both electronegativity, and hardness determine the maximum number of transferred electrons to inhibitors (ΔN_{max}). Here, all licorice components exhibited chemical reactivity and electron accepting ability (with the maximum charge transfer to Isoliquiritigenin molecule) as illustrated in Table 6**.** This is also consistent with the presence of carbonyl and hydroxyl functional groups in these components that can influence

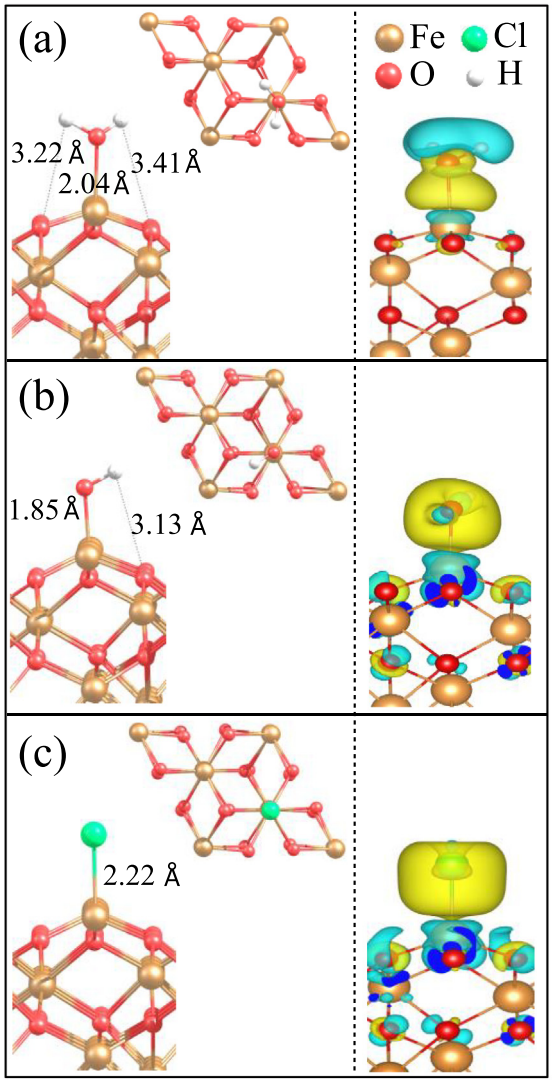

Fig. 9. Top and side views of the iron oxide surface with adsorbed (a) H_2O, (b) OH, and (c) Cl species. In the top view, the 2 × 2-unit cells are depicted. The right panels show the electron charge density difference for the adsorption of H_2O and OH calculated by DFT + U, PBE-D3 XC functional. The accumulation and depletion of electrons are represented by the yellow and cyan regions, respectively.

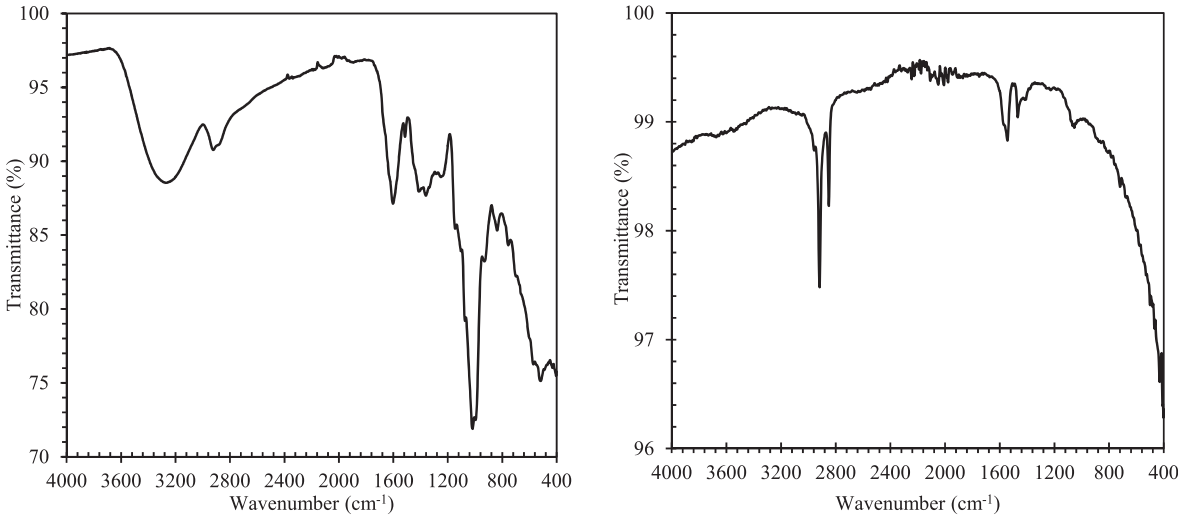

Fig. 8. FTIR spectrum of licorice extract powder (left) and FTIR-ATR spectrum of the steel surface dipped into the alkaline solution with 0.1% licorice extract for 24 h (right).

the inhibitor adsorption and enhance the charge transfer [77]. Furthermore, due to the intermolecular H-bonding in these components, a higher surface coverage during the adsorption process, and consequently higher inhibition efficiency is expected. The results indicated that licorice is a promising inhibitor of steel corrosion.

Iron oxide (Fe_2O_3) -the main chemical component of the outermost layer of the film formed on steel in an alkaline environment, as shown in Fig. 6**c** and Table 4, has been extensively studied in experiments [78,79] and theoretical calculations [80,81]. Here the (0001) surface was examined because it is the most stable surface orientation and occurs in naturally grown crystals [82,83]. When studying the inhibitor properties of compounds on an iron oxide surface, the effects of the solutioń s chemistry should be taken into consideration.

Here water, hydroxide and chloride molecules adsorption on the iron oxide surface were analyzed, by using DFT + U with PBE -D3 XC functional. The most stable configuration for the adsorption of H_2O, OH, and Cl species on iron oxide and the charge difference density are illustrated in Fig. 9. In the case of H_2O adsorption, the configuration of the adsorbed H_2O molecule remained almost unchanged and Fe-O bonding length became about 2.04 Å. This interaction pulls the Fe atom up by about 0.1 Å. Also, the interaction of the surface O layer and H atoms formed a 3.22 and 3.41 Å long bonds with the O layer moving downward about 0.07 Å (See Fig. 9**(a)**). Adsorption free energy and Bader charge transfer related to the interaction between H_2O and iron oxide were −0.45 eV and 0.10 e charge, respectively. In fact, the Fe surface atom lost 1.41 e charge to the O atom of H_2O and then the surface O layer got 1.51 e back which form bonds with H atoms. Thus, the charge density gets redistributed to decrease the electron–electron repulsion and causing the O layer to move toward the bulk.

The adsorption free energy (adsorption bond length) of OH and Cl were about −2.40 (1.85 Å) and −2.88 eV (2.22 Å), respectively, suggesting that the iron oxide is the OH and Cl species capturer

Table 5
Assignments of the most important bands of the ATR-FTIR spectra of the licorice extract powder and the steel surface exposed to the alkaline solution containing the licorice extract.

Wavenumbers (cm^{-1}) licorice extract	Wavenumbers (cm^{-1}) Steel surface	Assignments
3298 (3500–3000)		–OH st
2924, 2876	2918, 2850	$–CH_3$, $–CH_2$- st
1604,1516	1598, 1544	ArC-C
1410	1410	$–CH_3$ δ as, $–CH_2$- δ
1362	1376	$–CH_3$ δ s
1016	1052	ArC-O-C- al st s
836	878	ArC-H δ oop
740–705	ca. 720	$–CH_2$ δ, for C-$(CH_2)_n$-C n < 4

St: stretching, Ar: aromatic, δ: bending, s: symmetric, as: asymmetric, al: aliphatic, ip: in plane, oop: out of plane bending, n: number of CH_2 groups.

Table 6
Summary of licorice components properties: molecular weight (MW), number of H-bond donor/acceptor (HA/HD), water solubility (WS), and quantum chemical parameters, including the energy levels of the highest occupied molecular orbital (E_{HOMO}), lowest unoccupied molecular orbital (E_{LUMO}), energy gap (ΔE), dipole moment (μ), electronegativity (χ), global hardness (η) and the maximum number of electrons transferred (ΔN_{max}) based on B3LYP-D2 XC functional.

Name	PubChem ID	MW	HA	HD	WS (g/mol)	E_{HOMO} (eV)	E_{LUMO} (eV)	ΔE (eV)	μ (D)	χ (eV)	η (eV)	ΔN_{max}
Daidzein	5,281,708	254.28	4	2	−3.79	−6.32	−1.74	−4.58	2.47	4.03	2.29	0.88
Davidigenin	442,342	258.28	4	3	−3.05	−6.21	−1.84	−4.37	3.22	4.02	2.18	0.92
Dihydroformononetin	14,730,796	270.28	4	1	−3.48	−6.15	−1.66	−4.48	2.20	3.90	2.24	0.87
Enoxolone	10,114	470.69	3	2	−3.32	−6.49	−1.52	−4.97	3.62	4.00	2.48	0.80
Formononetin	5,280,378	268.27	4	1	−3.69	−6.20	−1.70	−4.49	2.01	3.95	2.24	0.88
Gancaonin C	6,450,959	354.36	6	4	−3.52	−6.16	−1.69	−4.46	3.58	3.93	2.23	0.87
Genistin	5,281,377	432.38	10	6	−2.75	−6.25	−1.54	−4.71	4.30	3.90	2.35	0.82
Glabridin	124,052	324.38	4	2	−3.64	−5.41	−0.86	−4.55	3.36	3.13	2.27	0.68
Glabrol	11,596,309	392.5	4	2	5.52	−6.23	−1.57	−4.66	3.22	3.90	2.33	0.83
Glabrone	5,317,652	336.34	5	2	−3.60	−5.67	−1.93	−3.74	2.84	3.80	1.87	1.01
Glyasperin A	5,481,963	422.47	6	4	−3.55	−5.97	−1.57	−4.40	4.73	3.77	2.20	0.85
Glycycoumarin	5,317,756	368.39	6	3	−3.64	−6.07	−2.10	−3.96	8.74	4.08	1.98	1.03
Glycyrin	480,787	382.41	6	2	−4.02	−6.10	−2.20	−3.90	7.24	4.15	1.95	1.06
Glycyrol	5,320,083	366.37	6	2	−3.93	−5.85	−1.83	−4.01	8.15	3.84	2.00	0.95
Glycyrrhetic Acid Glucuronide	161,800	646.81	8	5	−2.91	−6.26	−1.33	−4.92	6.86	3.80	2.46	0.77
Hispaglabridin B	15,228,661	390.4	4	1	−5.34	−5.38	−1.31	−4.07	3.92	3.34	2.03	0.82
Isoglycyrol	124,050	366.3	6	1	−3.71	−5.75	−1.77	−3.98	8.39	3.76	1.99	0.94
Isoliquiritigenin	638,278	256.26	4	3	−3.06	−6.15	−2.45	−3.69	4.88	4.30	1.84	1.16
Isoliquiritin	5,318,591	418.4	9	6	−2.56	−6.21	−2.25	−3.96	4.64	4.23	1.98	1.06
Licoagrochalcone A	11,099,375	324.37	4	3	−3.64	−6.11	−2.39	−3.72	4.93	4.25	1.86	1.14
Licochalcone D	10,473,311	354.4	5	3	4.216	−6.03	−2.08	−3.94	3.14	4.05	1.97	1.02
Licocoumarone	503,731	340.37	5	3	−3.85	−5.16	−1.01	−4.14	4.19	3.09	2.07	0.74
Licoflavone C	10,246,505	338.36	5	3	−3.71	−6.10	−1.61	−4.49	3.96	3.86	2.24	0.85
Licoflavonol	5,481,964	354.35	6	4	3.791	−6.02	−1.62	−4.39	3.82	3.82	2.19	0.87
Licoisoflavone B	5,481,234	352.34	6	3	−3.54	−5.63	−1.68	−3.95	4.48	3.65	1.97	0.92
Licoricesaponin B2	12,990,122	808.96	12	8	−2.89	−6.18	−0.98	−5.20	5.74	3.58	2.60	0.68
Licoricesaponin A3	14,187,172	985.08	19	11	−2.88	−6.35	−1.44	−4.90	7.94	3.90	2.45	0.79
Licoricesaponin C2	452,864	806.94	12	8	−2.89	−5.65	−0.93	−4.71	4.26	3.29	2.35	0.69
Licoricidin	480,865	424.53	5	3	−4.46	−5.62	−0.68	−4.93	3.28	3.15	2.46	0.63
Licuraside	639,005	550.51	13	8	−3.15	−6.24	−2.02	−4.21	3.39	4.13	2.10	0.98
Liquiritigenin	114,829	256.26	4	2	−3.24	−6.45	−1.68	−4.77	1.93	4.07	2.38	0.85
Liquiritin-apioside	10,076,238	550.51	13	7	−3.1	−6.55	−1.66	−4.89	3.62	4.10	2.44	0.83
Liquiritin	503,737	418.4	9	5	−3.35	−6.66	−1.76	−4.89	3.08	4.21	2.44	0.86
Ononin	442,813	430.40	9	4	−3.30	−6.25	−1.86	−4.39	3.00	4.06	2.19	0.92
Pinocembrin	68,071	256.26	4	2	−3.53	−6.48	−1.43	−5.04	2.56	3.96	2.52	0.78
Schaftoside	442,658	564.49	14	10	−2.84	−6.53	−1.83	−4.69	5.78	4.18	2.34	0.89
Shinflavanone	197,678	390.48	4	1	−6.22	−5.99	−1.66	−4.33	4.20	3.82	2.16	0.88
Shinpterocarpin	10,336,244	322.36	4	1	−3.69	−5.68	−1.08	−4.60	1.77	3.38	2.30	0.73
Sophoraflavanone-B	509,245	340.37	5	3	−3.56	−6.07	−1.35	−4.71	2.77	3.71	2.35	0.78
Topazolin	5,481,965	368.3	6	3	−3.63	−6.14	−1.68	−4.45	1.59	3.91	2.22	0.87

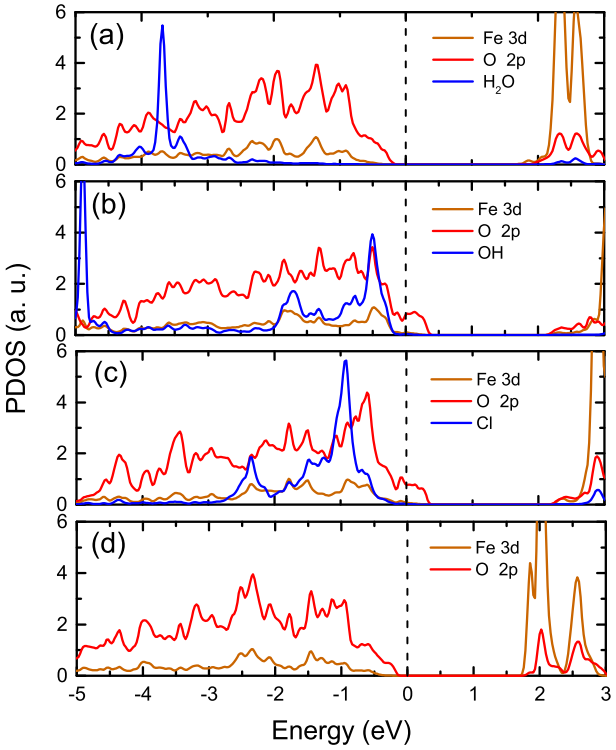

Fig. 10. Atomic orbital projected density of states (PDOS) for the most stable (a) H_2O, (b) OH, and (c) Cl adsorption at the iron oxide surface. (d) States of the 1 Fe and 3O atoms at the surface. The Fermi level is set to zero.

(see Fig. 9**(b) and 9(c)**). The adsorption of OH and Cl on iron oxide had comparable effects on the structure of the surface, pulling the outermost Fe atom out of the surface by up to 0.28 Å and 0.25 Å,

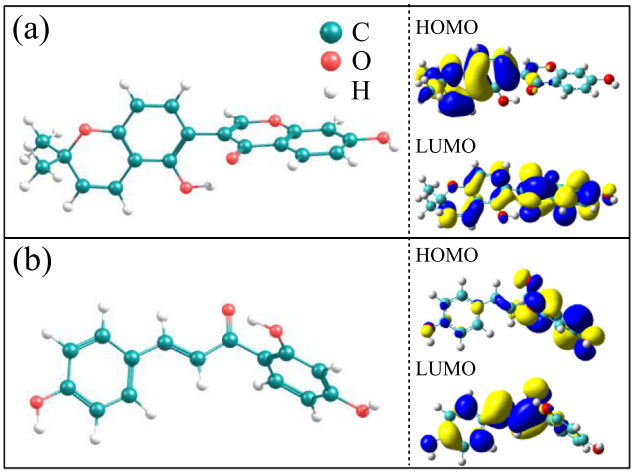

Fig. 11. (a) Glabrone (GBN) and (b) Isoliquiritigenin (ILQ) molecular structures. The right panels show the inhibitorś chemically active orbitals (HOMO and LUMO) based on B3LYP-D2 XC functional.

and moving the O layer toward the bulk by 0.08 Å and 0.11 Å, respectively. The Bader charge analysis showed that the OH gains 1.25 e and loses 0.63 e to the O layer through the H bond. Additionally, there was a charge transfer of about 0.64 e from the surface to Cl atom. The results showed that the adsorption of OH and Cl on pristine iron oxide change the surface structure, but the adsorption is not strong enough to induce diffusion of species into the oxide layer.

As illustrated in Fig. 10, the PDOS of the surface O layer -due to losing electrons to the surrounding atoms in the presence of OH and Cl adsorbates- shifted toward energies that are more positive and the structures became metallic.

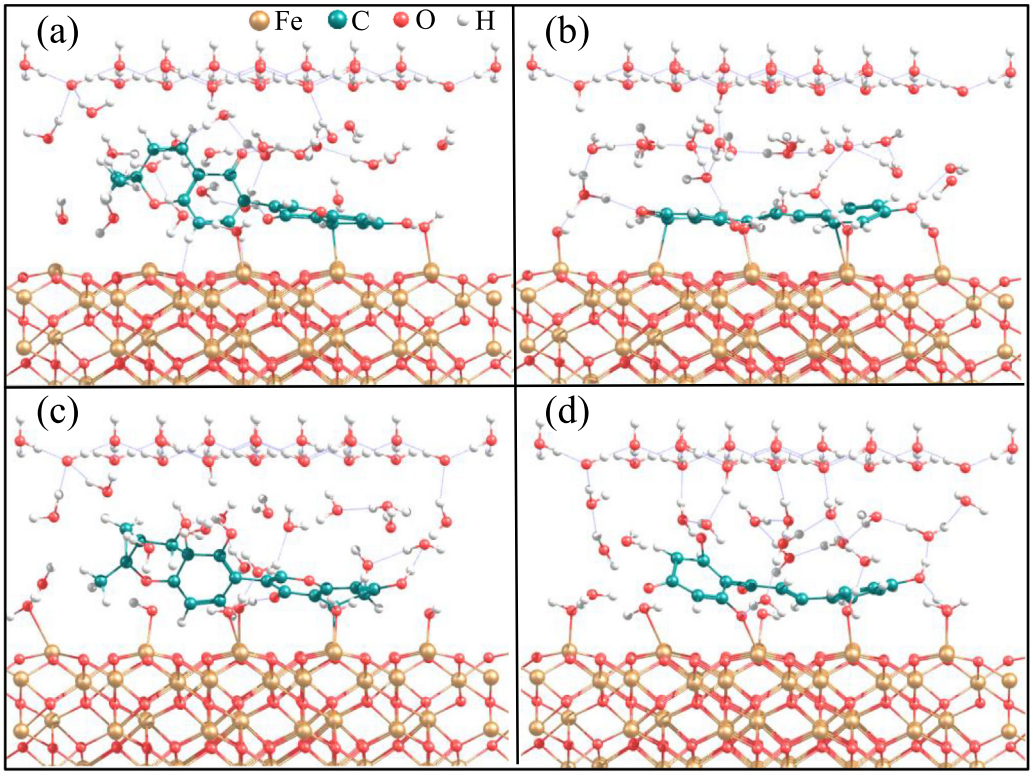

Fig. 12. The adsorption of (a) Glabrone (GBN) and (b) Isoliquiritigenin (ILQ) at the iron oxide surface under neutral conditions, and (c) GBN and (d) ILQ under alkaline conditions, obtained from 0.5 ps AIMD simulations.

Based on the lowest energy gap presented in Table 6, two components of licorice (Glabrone (GBN) and (b) Isoliquiritigenin (ILQ)) were selected for further investigation of inhibitor properties of this material on iron oxide. The molecular structure of GBN and LIQ are presented in Fig. 11**(a) and 11(b)**, respectively. The chemically active orbitals of GBN and ILQ are their HOMO and LUMO. The HOMO of GBN molecule is primarily distributed over the phenyl, pyran rings and methyl bonds. The LUMO is distributed at the side of = O bond. In the case of ILQ molecule, HOMO and LUMO are distributed around the = O bond and over it. Note that = O functional group has a larger contribution to LUMO.

To take into account the adsorption characteristics of the GBN and ILQ molecules on the iron oxide crystal surface under solvent conditions, AIMD calculation was employed. The structure of GBN and ILQ are shown in Fig. 12**(a) and 12(b)**, under neutral solvent conditions. The adsorption of molecules on the iron oxide surface was a multisite adsorption. In the presence of the water solvent, the H(O) atoms of H_2O molecules form hydrogen bonds (covalent bond) with O(Fe) atoms at the surface. Furthermore, H_2O molecules were revolved around GBN and ILQ molecules; interactions between H_2O molecules and the functional groups of molecules can occur through hydrogen bonds. Thus, to make the adsorption configuration stable, the molecular structure was deformed due to the influence of water molecules and the surface effect. After 0.5 ps of AIMD simulations, the ILQ molecule was adsorbed in a flat-lying orientation at the iron oxide surface, as expected from the delocalized electron density around the molecules. This orientation maximizes contact and surface coverage. Such behavior has been experimentally observed in organic molecular adsorption. [84,85]

In Fig. 13, the total energy and the root mean square (RMSD) deviation are shown for the studied structures. By analyzing the total energy profile and adsorption configuration of molecules at the iron oxide crystal surface under aqueous conditions, it was found that the degree of deformation of the GBN is much larger than that of the ILQ under aqueous solution conditions. This behavior can be related to the electronic properties of the molecule (for the non-covalent interaction) and the position of the most important functional group = O (for the covalent interaction). The adsorption configuration revealed that the O atom in the pyran (along the molecular backbone of GBN) avoids bonding with the iron oxide. The deformation of adsorbate on the lattice surfaces in solvent condition have been reported in the literature [86,87]. Furthermore, to understand the spatial distribution of charge upon molecules in the presence of water solvent and surface bonding, the Bader charge analysis was utilized. The Bader charge analysis reveals that GBN and ILQ lose 3.46 e and 0.36 e charge, respectively.

Fig. 12**(c) and 12(d)** show the GBN and ILQ adsorption configurations on the iron oxide in alkaline solutions, respectively. The adsorption of molecules at the iron oxide surface was affected by the intermolecular surface tension and degree of covalence and hydrogen bonding. The charge transfer from GBN and ILQ to surface and water molecules was about 0.38 and 0.57 e, respectively. As illustrated in Fig. 13, during the simulation time, total energies in alkaline solution were lower than that in neutral solution, which might be related to more changes in the configuration of molecules in alkaline solutions. Importantly, hydroxide as a highly reactive specie in alkaline solutions can attack GBN and ILQ molecules. The nucleophile attack by hydroxide in reaction with molecules makes the stability of O-H/C-C in aromatic rings weaker and thus

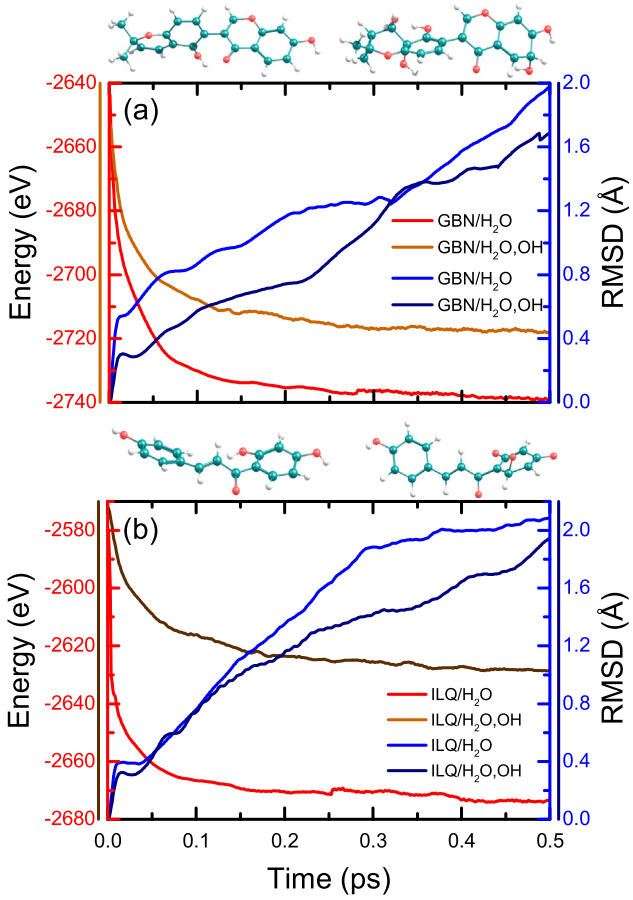

Fig. 13. The total energy and root mean square (RMSD) based on AIMD simulation for (a) Glabrone (GBN) and (b) Isoliquiritigenin (ILQ) at the iron oxide surface under neutral and alkaline conditions. Insets of molecular geometries show corresponding GBN/ILQ under neutral solution (left) and alkaline solution (right).

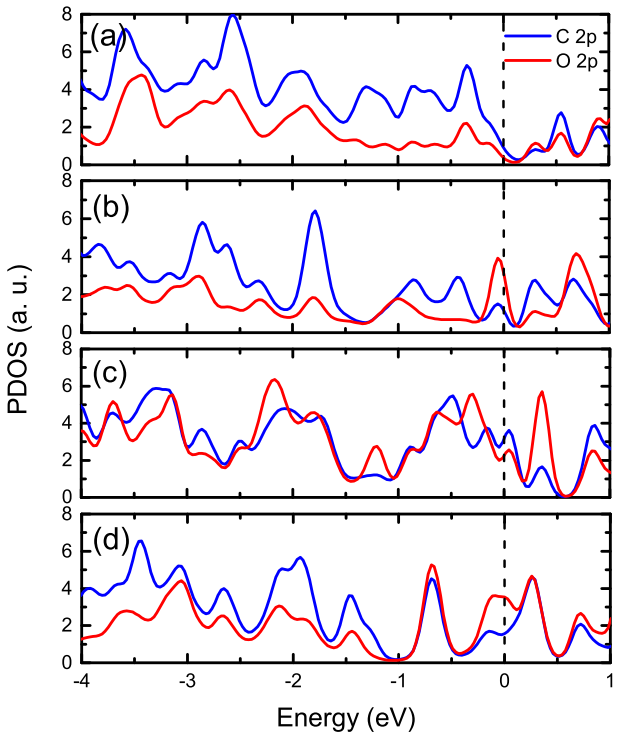

Fig. 14. Atomic orbital projected density of states (PDOS) of C and O components for (a) Glabrone (GBN) and (b) Isoliquiritigenin (ILQ) at the iron oxide surface under neutral conditions. PDOS for (c) GBN and (d) ILQ at the iron oxide surface under alkaline conditions. All energy levels of the PDOS refer to the corresponding Fermi level of iron oxide, which is set to zero.

backbones of the structures are modified to increase = O and OH content. In an appropriate concentration of licorice, the backbone rearrangement of chemical components may be energetically favorable for the adsorption on iron oxide surfaces

The projected density of the state (PDOS) of the p-orbitals of C and O atoms in GBN and ILQ molecules at the iron oxide crystal surface under solvent conditions is presented in Fig. 14. The broadening of the adsorbed C 2p occupied states showed a larger covalent contribution to the adsorption energy and charge transfer. It is worth mentioning that the = O and OH functional groups of components reveal the greatest contribution to inhibitor interactions and increase inhibition efficiency. In Fig. 14**(b)**, the strong interaction of the O of molecular ILQ significantly increased the DOS at the Fermi level, and led to stability of the absorbed structure, while the GBN required more time to achieve adequate stability. Moreover, Fig. 14**(c) and 14(d)** show the increased PDOS of O atoms indicating the formation of covalent bond with hydroxides in alkaline solution, and components adsorption on the iron oxide surface. The results revealed detailed information about the adsorption mechanism of licorice components under solvent conditions.

4. Conclusions

Licorice extract was introduced in this study as a green substance providing desirable corrosion inhibition for steel rebar in chloride-polluted concrete pore solution. The EIS data, extracted from modeling of the Nyquist and Bode diagrams, as well as polarization curves, indicated the superiority of the plant extract in the 0.1% concentration, obtaining a corrosion inhibition efficiency higher than 80%. By taking advantage of surface analysis methods, the inhibition function was linked to the role of the organic species existing in the licorice extract in strengthening the layer formed on the specimen surface in the alkaline condition. In other words, the FTIR and SEM-EDS methods could detect the presence of licorice on the surface and the XPS O 1 s, C 1 s and Fe 2p peaks deconvolution data confirmed the speculation made in the electrochemical assessment about deposition of organic molecules present in the plant extract on the surface oxide/hydroxide film. The quantum chemical parameters of licorice compounds, which mostly contain carbonyl and hydroxyl functional groups, indicated that this plant extract can be considered a promising inhibitor of steel corrosion in alkaline electrolyte. Moreover, the molecular adsorption type and the role of influential functional groups were studied through DFT calculations.

Declaration of Competing Interest

The authors declare that they have no known competing financial interests or personal relationships that could have appeared to influence the work reported in this paper.

Acknowledgements

This research was funded by the European Union Horizon 2020 research and innovation MSCA-IF-2019 programme under grant agreement No 892074 (NATCON project). Support from the Ministerio de Ciencia, Innovación y Universidades of Spain (RTI2018-096428-B-I00) is also acknowledged.

References

[1] S.A. Lee, K.-P. Park, J. Kim, K.Y. Ann, Sensitivity analysis for binders in concrete mix to the corrosion risk of steel embedment in chloride-bearing environments, Constr. Build. Mater. 251 (2020) 118944, https://doi.org/10.1016/j.conbuildmat.2020.118944.

[2] J.A. González, E. Otero, S. Feliu, A. Bautista, E. Ramírez, P. Rodríguez, W. López, Some considerations on the effect of chloride ions on the corrosion of steel reinforcements embedded in concrete structures, Mag. Concr. Res. 50 (3) (1998) 189–199, https://doi.org/10.1680/macr.1998.50.3.189.

[3] A. Bautista, J.C. Pomares, M.N. González, F. Velasco, Influence of the microstructure of TMT reinforcing bars on their corrosion behavior in concrete with chlorides, Constr. Build. Mater. 229 (2019) 116899, https://doi.org/10.1016/j.conbuildmat.2019.116899.

[4] A. Al-Negheimish, R.R. Hussain, A. Alhozaimy, D.D.N. Singh, Corrosion performance of hot-dip galvanized zinc-aluminum coated steel rebars in comparison to the conventional pure zinc coated rebars in concrete environment, Constr. Build. Mater. 274 (2021) 121921, https://doi.org/10.1016/j.conbuildmat.2020.121921.

[5] A. Bautista, E.C. Paredes, S.M. Alvarez, F. Velasco, Welded, sandblasted, stainless steel corrugated bars in non-carbonated and carbonated mortars: A 9-year corrosion study, Corros. Sci. 103 (2016) 363–372, https://doi.org/10.1016/j.corsci.2015.10.029.

[6] A. Goyal, E.K. Olorunnipa, H.S. Pouya, E. Ganjian, A.O. Olubanwo, Potential and current distribution across different layers of reinforcement in reinforced concrete cathodic protection system- A numerical study, Constr. Build. Mater. 262 (2020) 120580, https://doi.org/10.1016/j.conbuildmat.2020.120580.

[7] J.A. González, E. Ramírez, A. Bautista, Protection of steel embedded in chloride-containing concrete by means of inhibitors, Cem. Concr. Res. 28 (4) (1998) 577–589, https://doi.org/10.1016/S0008-8846(98)00014-3.

[8] P. B. Raja, S. Ghoreishiamiri, M. Ismail, Natural corrosion inhibitors for steel reinforcement in concrete — A review, Surf. Rev. Lett. 22 (2015) 1550040, DOI: 10.1142/S0218625X15500407.

[9] H. Yang, W. Li, X. Liu, A. Liu, P. Hang, R. Ding, T. Li, Y. Zhang, W. Wang, C. Xiong, Preparation of corrosion inhibitor loaded zeolites and corrosion resistance of carbon steel in simulated concrete pore solution, Constr. Build. Mater. 225 (2019) 90–98, https://doi.org/10.1016/j.conbuildmat.2019.07.141.

[10] H. Verbruggen, H. Terryn, I. De Graeve, Inhibitor evaluation in different simulated concrete pore solution for the protection of steel rebars, Constr. Build. Mater. 124 (2016) 887–896, https://doi.org/10.1016/j.conbuildmat.2016.07.115.

[11] S.B. Jiang, L.H. Jiang, Z.Y. Wang, M. Jin, S. Bai, S. Song, X. Yan, Deoxyribonucleic acid as an inhibitor for chloride-induced corrosion of reinforcing steel in simulated concrete pore solutions, Constr. Build. Mater. 150 (2017) 238–247, https://doi.org/10.1016/j.conbuildmat.2017.05.157.

[12] Y.P. Asmara, T. Kurniawan, A.G.E. Sutjipto, J. Jafar, Application of Plants Extracts as Green Corrosion Inhibitors for Steel in Concrete - A review, Indones, J. Sci. Technol. 3 (2) (2018) 158, https://doi.org/10.17509/ijost.v3i210.17509/ijost.v3i2.12760.

[13] P.B. Raja, M.G. Sethuraman, Natural products as corrosion inhibitor for metals in corrosive media — A review, Mater. Lett. 62 (1) (2008) 113–116, https://doi.org/10.1016/j.matlet.2007.04.079.

[14] L.T. Popoola, Organic green corrosion inhibitors (OGCIs): a critical review, Corros. Rev. 37 (2019) 71–102, https://doi.org/10.1515/corrrev-2018-0058.

[15] E. Salehi, R. Naderi, B. Ramezanzadeh, Synthesis and characterization of an effective organic/inorganic hybrid green corrosion inhibitive complex based on zinc acetate/Urtica Dioica, Appl. Surf. Sci. 396 (2017) 1499–1514, https://doi.org/10.1016/j.apsusc.2016.11.198.

[16] A.S. Abdulrahman, M. Ismail, M. Sakhawat Hussain, Corrosion inhibitors for steel reinforcement in concrete: A review, Sci. Res. Essays 6(20) (2011) 4152-4162, DOI: 10.5897/SRE11.1051.

[17] R. Anitha, S. Chitra, V. Hemapriya, I.M. Chung, S. Kim, M. Prabakara, Implications of eco-addition inhibitor to mitigate corrosion in reinforced steel embedded in concrete, Constr. Build. Mater. 213 (2019) 246–256, https://doi.org/10.1016/j.conbuildmat.2019.04.046.

[18] Y. Liu, Z. Song, W. Wang, L. Jiang, Y. Zhang, M. Guo, F. Song, N. Xu, Effect of ginger extract as green inhibitor on chloride-induced corrosion of carbon steel in simulated concrete pore solutions, J. Clean. Prod. 214 (2019) 298–307, https://doi.org/10.1016/j.jclepro.2018.12.299.

[19] Z. Zhang, H. Ba, Z. Wu, Sustainable corrosion inhibitor for steel in simulated concrete pore solution by maize gluten meal extract: Electrochemical and adsorption behavior studies, Constr. Build. Mater. 227 (2019) 117080, https://doi.org/10.1016/j.conbuildmat.2019.117080.

[20] S. Shanmugapriya, P. Prabhakar, S. Rajendran, Corrosion Resistance Property of Mild Steel in Simulated Concrete Pore Solution Prepared in Well Water by Using an Aqueous Extract of Turmeric, Mater. Today: Proc. 5 (2) (2018) 8789–8795, https://doi.org/10.1016/j.matpr.2017.12.307.

[21] D.B. Left, M. Zertoubi, S. Khoudali, M. Azzi, New Application of Chamaerops Humilis L. Extract as a Green Corrosion Inhibitor for Reinforcement Steel in a Simulated Carbonated Concrete Pore Solution, Port. Electrochim. Acta 36 (4) (2018) 249–257, https://doi.org/10.4152/pea.201804249.

[22] S.A. Asipita, M. Ismail, M. Z. AbdMajid, Z. AbdulMajid, C.S. Abdullah, J. Mirza, Green Bambusa Arundinacea leaves extract as a sustainable corrosion inhibitor in steel reinforced concrete, J. Clean. Prod. 67 (2014) 139e146, DOI: 10.1016/j.jclepro.2013.12.033.

[23] M. Ben Harb, S. Abubshait, N. Etteyeb, M. Kamoun, A. Dhouib, Olive leaf extract as a green corrosion inhibitor of reinforced concrete contaminated with seawater, Arab. J. Chem. 13 (3) (2020) 4846–4856, https://doi.org/10.1016/j.arabjc.2020.01.016.

[24] Q. Liu, Z. Song, H. Han, S. Donkor, L. Jiang, W. Wang, H. Chu, A novel green reinforcement corrosion inhibitor extracted from waste Platanus acerifolia leaves, Constr. Build. Mater. 260 (2020) 119695, https://doi.org/10.1016/j.conbuildmat.2020.119695.

[25] L. Račková, V. Jančinová, M. Petríková, K. Drábiková, R. Nosál', M. Štefek, D. Košťálová, N. Prónayová, M. Kováčová, Mechanism of anti-inflammatory action of liquorice extract and glycyrrhizin, Nat. Prod. Res. 21 (14) (2007) 1234–1241, https://doi.org/10.1080/14786410701371280.
[26] C.A. Coiffard, L.J. Coiffard, F.M. Peigne, Y.M. de Roeck-Holtzhauer, Monoammonium glycyrrhizinate stability in aqueous buffer solutions, J J. Sci. Food Agr. 77 (1998) 566–570, https://doi.org/10.1002/(SICI)1097-0010(199808)77:4<566::AID-JSFA84>3.0.CO;2-I.
[27] M. Alagawany, S.S. Elnesr, M.R. Farag, Use of liquorice *(Glycyrrhiza glabr*a) in poultry nutrition: Global impacts on performance, carcass and meat quality, Worlds Poult. Sci. J. 75 (2) (2019) 293–304, https://doi.org/10.1017/S0043933919000059.
[28] L. Siracusa, A. Saija, M. Cristani, F. Cimino, M. D'Arrigo, D. Trombetta, F. Rao, G. Ruberto, Phytocomplexes from liquorice *(Glycyrrhiza glabr*a L.) leaves — Chemical characterization and evaluation of their antioxidant, anti-genotoxic and anti-inflammatory activity, Fitoterapia 82 (4) (2011) 546–556, https://doi.org/10.1016/j.fitote.2011.01.009.
[29] A. Dal Bosco, S. Mattioli, Z. Matics, Z. Szendrő, Z. Gerencsér, A. Cartoni Mancinelli, M. Kovács, M. Cullere, C. Castellini, A. Dalle Zotte, The antioxidant effectiveness of liquorice (*Glycyrrhiza glabra* L.) extract administered as dietary supplementation and/or as a burger additive in rabbit meat, Meat Sci. 158 (2019) 107921, DOI: 10.1016/j.meatsci.2019.107921.
[30] E. Alibakhshi, M. Ramezanzadeh, G. Bahlakeh, B. Ramezanzadeh, M. Mahdavian, M. Motamedi, Glycyrrhiza glabra leaves extract as a green corrosion inhibitor for mild steel in 1 M hydrochloric acid solution: Experimental, molecular dynamics, Monte Carlo and quantum mechanics study, J. Molec. Liq. 255 (2018) 185–198, https://doi.org/10.1016/j.molliq.2018.01.144.
[31] E. Alibakhshi, M. Ramezanzadeh, S.A. Haddadi, G. Bahlakeh, B. Ramezanzadeh, M. Mahdavian, Persian Liquorice extract as a highly efficient sustainable corrosion inhibitor for mild steel in sodium chloride solution, J. Clean. Prod. 210 (2019) 660–672, https://doi.org/10.1016/j.jclepro.2018.11.053.
[32] V. Vorobyova, M. Skiba, A. Shakun, S. Nahirniak, Relationship between the inhibition and antioxidant properties of the plant and biomass wastes extracts – A Review, Int. J. Corros. Scale Inhib. 8 (2019) 150–178, https://doi.org/10.17675/2305-6894-2019-8-2-1.
[33] M.A. Deyab, Egyptian licorice extract as a green corrosion inhibitor for copper inhydrochloric acid solution, J. Ind. Eng. Chem. 22 (2015) 384–389, https://doi.org/10.1016/j.jiec.2014.07.036.
[34] M. Frisch, G. Trucks, H. Schlegel, G. Scuseria, M. Robb, J. Cheeseman, G. Scalmani, V. Barone, B. Mennucci, G. Petersson, ..., D. Fox, Gaussian 09, 2009, Revision C. 01, Gaussian, Inc., Wallingford CT.
[35] G. Kresse, D. Joubert, From ultrasoft pseudopotentials to the projector augmented-wave method, Phys. Rev. B 59 (3) (1999) 1758–1775, https://doi.org/10.1103/PhysRevB.59.1758.
[36] Y. Wang, J.P. Perdew, Correlation hole of the spin-polarized electron gas, with exact small-wave-vector and high-density scaling, Phys. Rev. B 44 (24) (1991) 13298–13307, https://doi.org/10.1103/PhysRevB.44.13298.
[37] G. Kresse, J. Furthmüller, Efficiency of ab-initio total energy calculations for metals and semiconductors using a plane-wave basis set, Comput. Mater. Sci. 6 (1) (1996) 15–50, https://doi.org/10.1016/0927-0256(96)00008-0.
[38] G. Kresse, J. Furthmüller, Efficient iterative schemes for ab initio total-energy calculations using a plane-wave basis set, Phys. Rev. B 54 (16) (1996) 11169–11186, https://doi.org/10.1103/PhysRevB.54.11169.
[39] K. Mathew, R. Sundararaman, K. Letchworth-Weaver, T.A. Arias, R.G. Hennig, Implicit solvation model for density-functional study of nanocrystal surfaces and reaction pathways, J. Chem. Phys. 140 (8) (2014) 084106, https://doi.org/10.1063/1.4865107.
[40] S. Grimme, J. Antony, S. Ehrlich, H. Krieg, A consistent and accurate ab initio parametrization of density functional dispersion correction (DFT-D) for the 94 elements H-Pu, J. Chem. Phys. 132 (15) (2010) 154104, https://doi.org/10.1063/1.3382344.
[41] S. Grimme, S. Ehrlich, L. Goerigk, Effect of the damping function in dispersion corrected density functional theory, J. Comput. Chem. 32 (7) (2011) 1456–1465, https://doi.org/10.1002/jcc.v32.710.1002/jcc.21759.
[42] V. Anisimov, F. Aryasetiawan, A. Lichtenstein, First-principles calculations of the electronic structure and spectra of strongly correlated systems: the LDA+ U method, J. Phys.- Condens. Matter. 9 (1997) 767–808.
[43] A. Lichtenstein, M. Katsnelson, Ab initio calculations of quasiparticle band structure in correlated systems: LDA++ approach, Phys. Rev. B. 57 (1998) 6884–6895, https://doi.org/10.1103/PhysRevB.57.6884.
[44] M.I. Katsnelson, A.I. Lichtenstein, First-principles calculations of magnetic interactions in correlated systems, Phys. Rev. B. 61 (13) (2000) 8906–8912, https://doi.org/10.1103/PhysRevB.61.8906.
[45] P. Liao, J.A. Keith, E.A. Carter, Water oxidation on pure and doped hematite (0001) surfaces: Prediction of Co and Ni as effective dopants for electrocatalysis, J. Amer. Chem. Soc. 134 (32) (2012) 13296–13309, https://doi.org/10.1021/ja301567f.
[46] J. Rossmeisl, K.D. Jensen, A.S. Petersen, L. Arnarson, A. Bagger, M. Escudero-Escribano, Realistic Cyclic Voltammograms from Ab Initio Simulations in Alkaline and Acidic Electrolytes, J. Phys. Chem. C 124 (37) (2020) 20055–20065, https://doi.org/10.1021/acs.jpcc.0c0436710.1021/acs.jpcc.0c04367.s001.
[47] M.H. Hansen, J. Rossmeisl, pH in grand canonical statistics of an electrochemical interface, J. Phys. Chem. C 120 (51) (2016) 29135–29143, https://doi.org/10.1021/acs.jpcc.6b0901910.1021/acs.jpcc.6b09019.s001.
[48] S. Nosé, A unified formulation of the constant temperature molecular dynamics methods, J. Chem. Phys. 81 (1) (1984) 511–519, https://doi.org/10.1063/1.447334.
[49] A. Popova, S. Raicheva, E. Sokolova, M. Christov, Frequency dispersion of interfacial impedance at mild steel corrosion in acid media in the presence of benzimidazole derivatives, Langmuir 12 (1996) 2083–2089, https://doi.org/10.1021/la950148+.
[50] U. Rammelt, G. Reinhard, The influence of surface roughness on the impedance data for iron electrodes in acid solutions, Corros. Sci. 27 (4) (1987) 373–382, https://doi.org/10.1016/0010-938X(87)90079-5.
[51] C. Hsu, F. Mansfeld, Concerning the conversion of the constant phase element parameter Y0 into a capacitance, Corrosion 57 (2001) 747–748, https://doi.org/10.5006/1.3280607.
[52] L. Kaghazchi, R. Naderi, B. Ramezanzadeh, Synergistic mild steel corrosion mitigation in sodium chloride-containing solution utilizing various mixtures of phytic acid molecules and Zn^{2+} ions, J. Molec. Liq. 323 (2021) 114589, https://doi.org/10.1016/j.molliq.2020.114589.
[53] M. Wu, H. Ma, J. Shi, Enhanced corrosion resistance of reinforcing steels in simulated concrete pore solution with low molybdate to chloride ratios, Cem. Concr. Compos. 110 (2020) 103589, https://doi.org/10.1016/j.cemconcomp.2020.103589.
[54] F. Zhi, L. Jiang, M. Jin, P. Xu, B. Xiao, Q. Jiang, L. Chen, Y. Gu, Inhibition effect and mechanism of polyacrylamide for steel corrosion in simulated concrete pore solution, Constr. Build. Mater. 259 (2020) 120425, https://doi.org/10.1016/j.conbuildmat.2020.120425.
[55] E. Salehi, R. Naderi, B. Ramezanzadeh, Improvement in the protective performance of epoxy ester coating through inclusion of an effective hybrid green corrosion inhibitive pigment, J. Taiwan Inst. Chem. Eng. 81 (2017) 391–405, https://doi.org/10.1016/j.jtice.2017.09.049.
[56] E.C. Paredes, A. Bautista, S.M. Alvarez, F. Velasco, Influence of the forming process of corrugated stainless steels on their corrosion behaviour in simulated pore solutions, Corros. Sci. 58 (2012) 52–61, https://doi.org/10.1016/j.corsci.2012.01.010.
[57] A.O. Yüce, G. Kardaş, Adsorption and inhibition effect of 2-thiohydantoin on mild steel corrosion in 0.1M HCl, Corros. Sci. 58 (2012) 86–94, https://doi.org/10.1016/j.corsci.2012.01.013.
[58] D. Prabhu, P. Rao, L. Coriandrum sativum, A novel green inhibitor for the corrosion inhibition of aluminium in 1.0 M phosphoric acid solution, J. Environ Chem. Eng. 1 (2013) 676–683, https://doi.org/10.1016/j.jece.2013.07.004.
[59] G. Greczynski, L. Hultman, X-ray photoelectron spectroscopy: Towards reliable binding energy referencing, Prog. Mater. Sci. 107 (2020) 100591, https://doi.org/10.1016/j.pmatsci.2019.100591.
[60] Yolanda Ng Lee, Rochel M. Lago, José Luis G. Fierro, Vicente Cortés, Fernando Sapiña, Eduardo Martínez, Surface properties and catalytic performance for ethane combustion of $La_{1-x}K_xMnO_{3+\delta}$ perovskites, Appl. Catal. A- Gen. 207 (1-2) (2001) 17–24, https://doi.org/10.1016/S0926-860X(00)00610-4.
[61] Yazhou Zhao, Tao Pan, Xiaotong Yu, Da Chen, Corrosion inhibition efficiency of triethanolammonium dodecylbenzene sulfonate on Q235 carbon steel in simulated concrete pore solution, Corros. Sci. 158 (2019) 108097, https://doi.org/10.1016/j.corsci.2019.108097.
[62] D. Xiao, K. Dai, Y. Qu, Y. Yin, H. Chen, Hydrothermal synthesis of α-Fe_2O_3/g-C_3N_4 composite and its efficient photocatalytic reduction of Cr(VI) under visible light, Appl. Surf. Sci. 358 (2015) 181–187, https://doi.org/10.1016/j.apsusc.2015.09.042.
[63] Xiangnan Chen, Xiaohui Wang, De Fang, A review on C1s XPS-spectra for some kinds of carbon materials, Eur. Mat. Res. 28 (12) (2020) 1048–1058, https://doi.org/10.1080/1536383X.2020.1794851.
[64] P. Kaspar, D. Sobola, R. Dallaev, S. Ramazanov, A. Nebojsa, S. Rezaee, L. Grmela, Characterization of Fe_2O_3 thin film on highly oriented pyrolytic graphite by AFM, Ellipsometry and XPS, Appl. Surf. Sci. 493 (2019) 673–678, https://doi.org/10.1016/j.apsusc.2019.07.058.
[65] Dirk Rosenthal, Marina Ruta, Robert Schlögl, Lioubov Kiwi-Minsker, Combined XPS and TPD study of oxygen-functionalized carbon nanofibers grown on sintered metal fibers, Carbon 48 (6) (2010) 1835–1843, https://doi.org/10.1016/j.carbon.2010.01.029.
[66] M. Lu, H. Cheng, Y. Yang, A comparison of solid electrolyte interphase (SEI) on the artificial graphite anode of the aged and cycled commercial lithium ion cells, Electrochim. Acta 53 (9) (2008) 3539–3546, https://doi.org/10.1016/j.electacta.2007.09.062.
[67] F. Cao, J. Wei, J. Dong, W. Ke, The corrosion inhibition effect of phytic acid on 20SiMn steel in simulated carbonated concrete pore solution, Corros. Sci. 100 (2015) 365–376, https://doi.org/10.1016/j.corsci.2015.08.020.
[68] S. Chitravathi, Surender Kumar, N. Munichandraiah, NiFe-layered double hydroxides: a bifunctional O_2 electrode catalyst for non-aqueous Li–O_2 batteries, RSC Adv. 6 (105) (2016) 103106–103115, https://doi.org/10.1039/C6RA19054E.
[69] N. Likhanova, N. Nava, O. Olivares-Xometl, M. Domínguez-Aguilar, P. Arellanes-Lozada, I. Lijanova, J. Arriola-Morales, L. Lartundo-Rojas, Corrosion Evaluation of Pipeline Steel API 5L X52 in partially deaerated Produced Water with High Chloride Content, Int. J. Electrochem. Sci. 13 (2018) 7949–7967, https://doi.org/10.20964/2018.08.13.
[70] M. Fernández-Alvarez, F. Velasco, A. Bautista, Performance of ultraviolet exposed epoxy poder coatings functionalized with silica by hot mixing, J. Mater. Res. Technol. 10 (2021) 1042–1057, https://doi.org/10.1016/j.jmrt.2020.12.094.

[71] A. Barbosa, L. Da Silva, J. Abenojar, J. Del Real, R. Paiva, A. Ochsner, Kinetic analysis and characterization of an epoxy/cork adhesive, Thermochim. Acta 604 (2015) 52–60, https://doi.org/10.1016/j.tca.2015.01.025.
[72] M. Ebrahimzadeh, M. Gholami, M. Momeni, A. Kosari, M. Moayed, A. Davoodi, Theoretical and experimental investigations on corrosion control of 65Cu–35Zn brass in nitric acid by two thiophenol derivatives, Appl. Surf. Sci. 332 (2015) 384–392, https://doi.org/10.1016/j.apsusc.2015.01.178.
[73] T. Chaitra, K. Mohana, H. Tandon, Thermodynamic, electrochemical and quantum chemical evaluation of some triazole Schiff bases as mild steel corrosion inhibitors in acid media, J. Mol. Liq. 211 (2015) 1026–1038, https://doi.org/10.1016/j.molliq.2015.08.031.
[74] B. El Ibrahimi, A. Soumoue, A. Jmiai, H. Bourzi, R. Oukhrib, K. Mouaden, S. El Issami, L. Bazzi, Computational study of some triazole derivatives (un-and protonated forms) and their copper complexes in corrosion inhibition process, J. Mol. Struct. 1125 (2016) 93–102, https://doi.org/10.1016/j.molstruc.2016.06.057.
[75] N. Wazzan, DFT calculations of thiosemicarbazide, arylisothiocynates, and 1-aryl-2, 5-dithiohydrazodicarbonamides as corrosion inhibitors of copper in an aqueous chloride solution, J. Ind. Eng. Chem. 26 (2015) 291–308, https://doi.org/10.1016/j.jiec.2014.11.043.
[76] M. Radovanović, Z. Tasić, M. Mihajlović, A. Simonović, M. Antonijević, Electrochemical and DFT studies of brass corrosion inhibition in 3% NaCl in the presence of environmentally friendly compounds, Sci. Rep. 9 (2019) 1–16, https://doi.org/10.1038/s41598-019-52635-2.
[77] Chiara Gattinoni, James P. Ewen, Daniele Dini, Adsorption of surfactants on α-Fe_2O_3 (0001): a density functional theory study, J. Phys. Chem. C 122 (36) (2018) 20817–20826, https://doi.org/10.1021/acs.jpcc.8b0589910.1021/acs.jpcc.8b05899.s002.
[78] C. Örnek, C. Leygraf, J. Pan, Passive film characterisation of duplex stainless steel using scanning Kelvin probe force microscopy in combination with electrochemical measurements, npj Mater, Degrad. 3 (2019) 1–8, https://doi.org/10.1038/s41529-019-0071-8.
[79] P. Ghods, O.B. Isgor, J.R. Brown, F. Bensebaa, D. Kingston, XPS depth profiling study on the passive oxide film of carbon steel in saturated calcium hydroxide solution and the effect of chloride on the film properties, Appl. Surf. Sci. 257 (10) (2011) 4669–4677, https://doi.org/10.1016/j.apsusc.2010.12.120.
[80] Man-Fai Ng, Daniel John Blackwood, Hongmei Jin, Teck Leong Tan, DFT Study of Oxygen Reduction Reaction on Chromia and Hematite: Insights into Corrosion Inhibition, J. Phys. Chem. C 124 (25) (2020) 13799–13808, https://doi.org/10.1021/acs.jpcc.0c0355910.1021/acs.jpcc.0c03559.s001.
[81] H. DorMohammadi, Q. Pang, P. Murkute, L. Árnadóttir, O. Isgor, Investigation of chloride-induced depassivation of iron in alkaline media by reactive force field molecular dynamics, npj Mater, Degrad. 3 (2019) 1–11, https://doi.org/10.1038/s41529-019-0081-6.
[82] Robert J. Lad, Victor E. Henrich, Structure of α-Fe_2O_3 single crystal surfaces following Ar+ ion bombardment and annealing in O_2, Surf. Sci. 193 (1-2) (1988) 81–93, https://doi.org/10.1016/0039-6028(88)90324-X.
[83] S. Guiance, D. Coria, I. Irurzun, E. Mola, 2016. A Preliminary DFT study of the adsorption and dissociation of CH_4, SO_2 and O_2 reactions on Cr_2O_3(0001). arXiv preprint arXiv:1612.00672.
[84] David Ebuka Arthur, Computational and experimental study on corrosion inhibition potential of the synergistic 1: 1 combination of Arabic and cashew gums on mild steel, Pet. Res. 5 (2) (2020) 170–180, https://doi.org/10.1016/j.ptlrs.2020.01.002.
[85] Eléa Vernack, Dominique Costa, Philippe Tingaut, Philippe Marcus, DFT studies of 2-mercaptobenzothiazole and 2-mercaptobenzimidazole as corrosion inhibitors for copper, Corros. Sci. 174 (2020) 108840, https://doi.org/10.1016/j.corsci.2020.108840.
[86] R. Tan, Z. Lv, J. Tang, Y. Wang, J. Guo, L. Li, Theoretical study of the adsorption characteristics and the environmental influence of ornidazole on the surface of photocatalyst TiO_2, Sci. Rep. 9 (2019) 1–8, https://doi.org/10.1038/s41598-019-47379-y.
[87] S. El Arrouji, K. Karrouchi, A. Berisha, K. Alaoui, I. Warad, Z. Rais, S. Radi, M. Taleb, M. Ansar, A. Zarrouk, New pyrazole derivatives as effective corrosion inhibitors on steel-electrolyte interface in 1 M HCl: Electrochemical, surface morphological (SEM) and computational analysis, Colloid. Surface. A 604 (2020), https://doi.org/10.1016/j.colsurfa.2020.125325 125325.